

Faculty of Physics and Astronomy
Ruprecht-Karls-University Heidelberg

MASTER'S THESIS

in Physics

submitted by

Nicolas Robert Kahne

born in Kaiserslautern

February 2024

Optimization of inductance matching for current-sensor dc-SQUIDs to readout metallic magnetic calorimeters

This Master thesis was carried out by Nicolas Robert Kahne
at the Kirchhoff-Institute for Physics
under the supervision of
Prof. Dr. C. Enss

This thesis describes the design and development of a current-sensor dc-SQUID, optimized for the readout of metallic magnetic calorimeter based particle detectors. Maximizing the energy resolution of the detector is achieved by minimizing the intrinsic noise of the SQUID and by matching the input inductance of the SQUID with the inductance of the detector. This was realized by adding a second turn to the input coil of a previously produced SQUID to match the pickup coil inductance $L_p = 6.65 \text{ pH}$ of the maXs100 detector, which is currently being developed in this working group. To mitigate resonant structures in the SQUID dynamics, two new damping techniques were employed. These consisted of gold layers sputtered both atop the feed lines and between SQUID loop and input coil, with the latter representing a lossy microstrip line. Successful damping was achieved by the former as it resulted in substantially smoother current-voltage characteristics. The noise measurements of the new SQUID with various combinations of the damping scheme were performed at a temperature of 10 mK . These yielded up to $\sqrt{S_{\Phi_s,w}} = 0.22 \mu\Phi_0/\sqrt{\text{Hz}}$ for the frequency independent contribution, whereas the $1/f$ component was as low as $\sqrt{S_{\Phi_s,1/f}} = 2.0 \mu\Phi_0/\sqrt{\text{Hz}}$, thus being comparable to previous low-noise SQUIDs from this working group.

Optimierung der Induktivitätsanpassung von Stromsensor-dc-SQUIDs zur Auslese metallischer magnetischer Kalorimeter

In der vorliegenden Arbeit wird das Design und die Entwicklung eines Stromsensor-dc-SQUIDs beschrieben, welches hinsichtlich der Auslese von Teilchendetektoren auf Basis metallischer magnetischer Kalorimeter optimiert wurde. Die Maximierung der Energieauflösung des Detektors wird durch Minimierung des intrinsischen SQUID Rauschens und durch die Anpassung der Eingangsinduktivität des SQUIDs an die Induktivität des Detektors erreicht. Dies wurde durch das Erweitern der Einkoppelspule eines zuvor hergestellten SQUIDs mithilfe einer zweiten Windung realisiert, sodass diese der Induktivität der Detektorspule $L_p = 6.65 \text{ pH}$ des maXs100-Detektors angepasst wird, welcher derzeit in dieser Arbeitsgruppe entwickelt wird. Um Resonanzstrukturen in den SQUID Kennlinien zu minimieren, wurden zwei neue Dämpfungstechniken eingesetzt. Diese bestanden aus Goldschichten, die sowohl auf den Zuleitungen als auch zwischen der SQUID-Schleife und der Einkoppelspule aufgetragen wurden, wobei letzteres eine verlustreiche Mikrostreifenleitung darstellt. Eine erfolgreiche Dämpfung wurde durch die erstgenannte Methode erreicht, was durch wesentlich glattere Strom-Spannungs-Kennlinien demonstriert werden konnte. Die Rauschmessungen wurden für das neue SQUID mit verschiedenen Kombinationen der Dämpfungsmethoden bei einer Temperatur von 10 mK durchgeführt. Diese ergaben bis zu $\sqrt{S_{\Phi_s,w}} = 0.22 \mu\Phi_0/\sqrt{\text{Hz}}$ für den frequenzunabhängigen Beitrag, während für die $1/f$ -Komponente ein Wert von $\sqrt{S_{\Phi_s,1/f}} = 2.0 \mu\Phi_0/\sqrt{\text{Hz}}$ erreicht werden konnte, was vergleichbar mit früheren rauscharmen SQUIDs aus dieser Arbeitsgruppe ist.

Contents

1	Introduction	1
2	Theoretical Background	5
2.1	Josephson junctions	5
2.1.1	Josephson effect	5
2.1.2	Josephson Junctions in a Magnetic Field	9
2.1.3	RCSJ Model	11
2.2	dc-SQUIDs	15
2.2.1	Zero Voltage State	15
2.2.2	Voltage State	18
2.2.3	Optimal Parameters	20
2.2.4	Noise	21
2.2.5	Parasitic Resonances	22
3	Experimental Methods	27
3.1	Practical dc-SQUIDs	27
3.1.1	Gradiometer	29
3.2	Operation of a dc-SQUID	30
3.2.1	Flux-Locked Loop	31
3.2.2	Two-Stage Configuration	33
3.3	Metallic Magnetic Calorimeters	36
3.3.1	Extrinsic Energy Sensitivity	38

4 dc-SQUID Design	41
4.1 dc-SQUID with a Two-Turn Input Coil	41
4.2 Damping Methods	45
4.2.1 Lossy Input Coil	46
4.2.2 Inductive Damping	47
5 Experimental Results	51
5.1 Characteristic dc-SQUID Parameters	51
5.2 Input Coil Inductance	55
5.3 Resonance Behavior	57
5.4 Noise Performance	62
5.5 Energy Sensitivity	66
6 Summary and Outlook	69
Bibliography	73

1. Introduction

Particle detectors requiring a high energy-independent resolution combined with a large bandwidth have been successfully realized in the form of cryogenic metallic magnetic calorimeters (MMC) [Ens05]. These high-precision low-temperature detectors are used in a broad range of applications, such as for mass spectrometry of heavy particles [Hen17], spectroscopy of highly charged heavy ions [?] or the investigation of the mass of the electron-neutrino [Gas17]. Their working principle is based on the conversion of the energy of an incoming particle into a magnetic flux change. This is realized by the use of a paramagnetic sensor in a weak magnetic field, which experiences a temperature change upon the absorption of an incoming particle through an absorber that is thermally coupled to the sensor. The temperature increase is accompanied by a change in magnetization of the paramagnet, which creates a flux change that is read out by a direct current superconducting quantum interference device (dc-SQUID). SQUIDs represent highly sensitive state of the art magnetometers with a broad bandwidth. The SQUID can couple to the MMC via a flux transformer setup, where its input coil is connected to the pickup coil of the MMC experiencing the initial flux change $\Delta\Phi$. The induced current change creates a flux change $\Delta\Phi_s$ in the input coil that couples into the superconducting SQUID loop, which is intersected by two Josephson junctions. A current-biased dc-SQUID produces a finite voltage across both arms of the loop upon a magnetic flux change. The resulting non-linear current-voltage-characteristics require a broadband FLL feedback readout setup to linearize and amplify the output voltage. To reduce the noise contribution of the feedback electronics, a secondary SQUID is implemented to act as a low temperature preamplifier. The apparent noise in the current-sensor SQUID, however, couples into the MMC, which adds to the intrinsic noise of the detector.

For the detectors developed in this working group, this added noise dominates the flux noise spectrum above a few kHz, whereas $1/f$ noise of doped Erbium atoms and thermodynamic energy fluctuations are mostly responsible for low frequency noise [Kem18]. The energy resolution ΔE_{FWHM} , which can be described by the signal to noise ratio, is therefore negatively affected by the SQUID readout chain. To quantify this effect, we use the extrinsic energy sensitivity ϵ_p given by the intrinsic noise of the SQUID S_{Φ_s} and the inverse of the flux-to-flux coupling $\Delta\Phi_s/\Delta\Phi$.

The objective of this thesis was to optimize the coupling between the SQUID and the X-ray detector maXs100 developed in this working group. This was realized by adding a second turn to the input coil of the detector SQUID to match its inductance with the one of the pickup coil, as this maximizes the coupling $\Delta\Phi_s/\Delta\Phi$. We further

investigated the resonance and noise behavior to assess that the new design leads to an overall reduction of ϵ_p .

In chapter 2 we first introduce the theoretical framework of Josephson junctions that is needed to describe the working principle of a dc-SQUID. As such, we cover macroscopic quantum effects such as the Josephson effect and flux quantization. These explain the characteristic properties of Josephson junctions, which are realized as SIS tunnel contacts in this working group. To motivate the use of SQUIDs, it is essential to investigate the behavior of the junction in an external magnetic field. Following this, we cover the general aspects of dc-SQUIDs including their characteristics and noise behavior. Lastly, we discuss parasitic LC resonances arising from geometric properties of the SQUID circuit.

Chapter 3 covers more in depth the realization of practical SQUIDs and how their parameters are chosen to optimize the performance. The importance of using a second stage SQUID representing a low temperature preamplifier is demonstrated, as it significantly improves the signal to noise ratio. The last part of the chapter gives a short introduction to MMCs, summarizing their core features followed by a brief overview of the extrinsic energy sensitivity regarding the SQUID-based readout, which motivates the needed adjustment of the input coil to the pickup coil of the detector, thereby greatly improving the coupling between SQUID and detector.

In chapter 4 we present the new SQUID design based on the SQUID developed in [Bau22], where a second turn has been added to the input coil with the premise to better match the pickup coil inductance $L_p = 6.65\text{ nH}$ of the maXs100 detector. Further optimal design parameters are discussed which ensure minimal flux noise as well as smooth current-voltage-characteristics (IVCs). To mitigate the influence of resonances, various damping techniques are applied, such as shunting the LC circuits with resistors. We discuss new damping approaches involving insulated gold layers distributed over the feed lines as well as placing an added gold layer beneath the input coil, which represents a lossy microstrip line.

The measured characteristic properties of the new SQUID design are presented in chapter 5. Following this, we discuss the measurement of the input coil inductance and compare it to the expected value. To gain insight into the resonance behavior, we measured the IVC's of various new SQUID variants containing different combinations of the damping schemes described in chapter 3. Additionally, a SQUID without input coil has been tested for comparison to help identify input coil related resonances. The chapter ends with the discussion of the noise measurements, which was conducted with variants containing the lossy microstrip input coil, both with and without feed lines with overlaying gold layers. Lastly, the measured noise values are used to obtain intrinsic and extrinsic energy sensitivities, which are compared among the measured

variants. We conclude whether the new design is better suited for the readout of the maXs100 detector and propose possible improvements for future works.

2. Theoretical Background

This chapter provides a short introduction into Josephson junctions and their role in dc-SQUIDs (**d**irect **c**urrent **S**uperconducting **Q**Uantum **I**nterference **D**evice), which will be the main focus of this thesis. We start with a brief overview on macroscopic quantum phenomena such as the Josephson effect and explain the general working principle of superconductor-isolator-superconductor (SIS) tunnel contacts, followed by a summary of their basic properties. These tunnel contacts form the theoretical framework to describe the SQUIDs, which are developed in this group and optimized within the scope of this thesis. Lastly, we will take a closer look into their parasitic resonance behavior and investigate chapter different methods to reduce the quality factors. We will closely follow the derivations from the textbooks [Cla04] and [Gro16].

2.1 Josephson junctions

The *Josephson junction* named after Brian D. Josephson consists of two identical superconductors weakly coupled to each other. In the case of the junctions produced in this working group, such coupling is realized through a few nm thin insulating layer between the superconducting electrodes. Consequently, they are also referred to as SIS junctions. The resulting trilayer structure typically consists of Nb/Al-AlO_x/Nb, with niobium being used for the superconductors and the insulating layer being provided by the aluminum oxide. Both superconductors are attributed with a macroscopic quantum mechanical phase θ_1 and θ_2 , respectively. The macroscopic nature of these phases will be explained in subsection 2.1.1. A schematic structure is shown in figure 2.1. By connecting the tunnel junction to a current source they exhibit a non-trivial current-voltage behavior, which will be covered in the following.

2.1.1 Josephson effect

According to the BCS theory developed by Bardeen, Cooper and Schrieffer in 1957 [Bar57], electrons in a superconductor form pairs below a material dependent critical temperature T_c . These composite particles are also referred to as *Cooper pairs* and they represent the superconducting charge carriers with twice the mass and charge of a single electron. Their dissipationless flow causes the current to have zero dc-resistance, which is alongside the Meissner-Ochsenfeld effect [Mei33] the most characteristic feature of a superconductor. The latter describes magnetic field expulsion at the temperature T_c , provided the external magnetic field is smaller than a

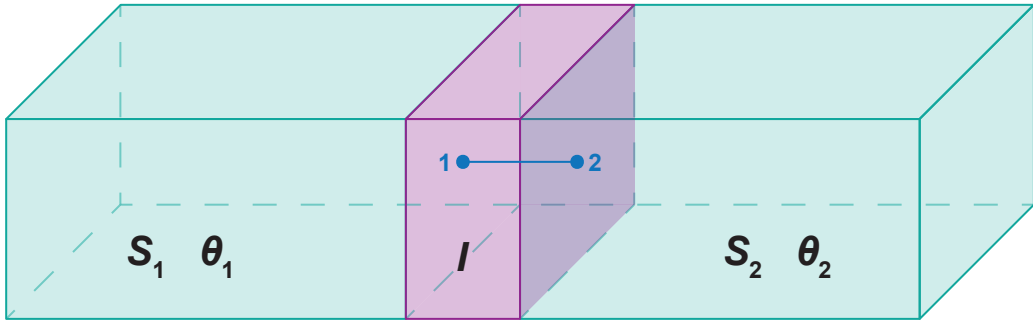


Figure 2.1: Schematic of a Josephson (SIS) junction. Both superconducting electrodes S_1 and S_2 are weakly coupled with each other through a thin tunnel barrier I . θ_1 and θ_2 represent the macroscopic phases of each superconductor.

critical field B_c . Further details on the microscopic theory of superconductivity can be found in [Bar57] and [Gin50].

For temperatures $T < T_c$ ($T_c = 9.3\text{ K}$ [Ina80]) Cooper pairs are able to tunnel across a Nb/Al-AlO_x/Nb Josephson junction despite the insulating barrier. In fact, their tunneling behavior resembles that of a single electron, which can be motivated by the *Macroscopic Quantum Model* that was formulated by Fritz London in 1953. This model heavily focuses on the quantum mechanical phase θ of a Cooper pair, whose macroscopic nature can be understood by the following arguments. On one hand, the distance between both electrons in a Cooper pair is approximately 10 to 1000 nm which is significantly larger than the spacing between Cooper pairs, resulting in strongly overlapping wave functions. On the other hand, Cooper pairs have to obey Bose-Einstein statistics due to their total spin of 0. Thus, all Cooper pairs share the same ground state, and as a consequence, the energies and temporal evolutions of the phases are equal. These two effects lead to what is known as *phase-lock* [Gro16]. The phases of neighboring pairs synchronize such that this quantum mechanical property now holds on a macroscopic scale. This gives rise to the phase-dependent macroscopic wave function

$$\Psi(\mathbf{r}, t) = \Psi_0(\mathbf{r}, t)e^{i\theta(\mathbf{r}, t)} , \quad (2.1)$$

which describes all charge carriers of a bulk superconductor. Here, the charge carrier density is given by $|\Psi_0(\mathbf{r}, t)|^2 = n_s$. The phase of the Cooper pair ensemble depends on the time t and the position \mathbf{r} . As a result of sharing the same phase, both electrons of a Cooper pair consequently possess the same tunneling probability as an individual electron, enabling the supercurrent. This coherence phenomenon is referred to as the *Josephson effect* [Jos62]. Another significant consequence of the

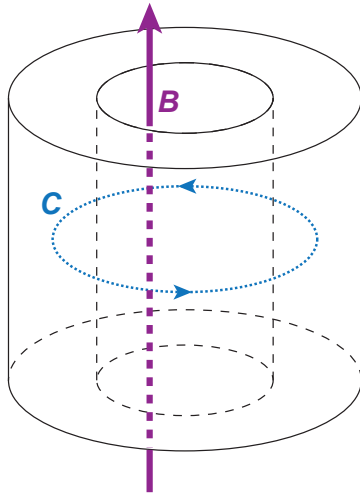


Figure 2.2: Superconducting ring-shaped cylinder threaded by an external magnetic field. By applying the field at low temperatures, shielding currents arise to expel the field from the superconductor. Upon turning off the external field the shielding currents will remain due to the lack of resistance, causing magnetic flux to be trapped. The dotted blue path C is situated at the center of the cylinder wall, which we assume to be current-free due to the London penetration depth λ_L being much smaller than the thickness of the cylinder wall.

macroscopic quantum model is flux quantization.

This phenomenon can be explained through the capture of an external magnetic flux within a superconducting cylinder (see figure 2.2). The wave function must remain unchanged after circumnavigating the cylinder due to $e^{i\theta} = e^{i\theta+2\pi n}$. As a result, upon integrating along the current-free center of the cylinder wall (path C), the following equation holds for the captured flux [Dea61]

$$\Phi = \frac{h}{q_s} n = \frac{h}{2e} n \equiv \Phi_0 n . \quad (2.2)$$

Here, $n \in \mathbb{Z}$ and $\Phi_0 = 2.07 \times 10^{-15} \text{ T m}^2$ [Tie21] represents the so-called magnetic flux quantum. The captured flux is thus quantized, a consequence solely arising from the macroscopic nature of the phase. This quantity plays a crucial role in the theoretical description of Josephson junctions.

The current and voltage behavior in a SIS junction is described by the *Josephson equations*. Crucial to this description is a critical current I_c that is linearly proportional to the applied current I , which marks the boundary between two operational modes; the zero-voltage state and the voltage state. Additionally, due to the macroscopic nature of the phase, I oscillates with the gauge-invariant phase difference φ , leading to the **first Josephson equation** [Jos65]

$$I_s = I_c \sin(\varphi) . \quad (2.3)$$

The critical current I_c is proportional to the coupling strength κ , which describes the overlap of the wave functions Ψ_1 and Ψ_2 within the insulating layer. The relationship is given by

$$I_c = \frac{4e\kappa V n_s}{\hbar} , \quad (2.4)$$

where V represents the volume of the superconducting electrode and e denotes the elementary charge of an electron. We assume that the Cooper pair density n_s of the two superconductors S_1 and S_2 is identical, meaning $n_{s1} = n_{s2} = n_s$.

The gauge-invariant phase difference refers to the phases θ_1 and θ_2 of the respective electrodes at the boundary of the insulating layer (positions 1 and 2, see figure 2.1). Taking into account possible external electromagnetic fields within the barrier, the general form using the vector potential \mathbf{A} is given by [Gro16]

$$\varphi(\mathbf{r}, t) = \theta_2(\mathbf{r}, t) - \theta_1(\mathbf{r}, t) - \frac{2\pi}{\Phi_0} \int_1^2 \mathbf{A}(\mathbf{r}, t) \cdot d\mathbf{l} . \quad (2.5)$$

Assuming a constant supercurrent density J_s across the junction, taking the time derivative of equation (2.5) yields the **second Josephson equation** [Jos65]

$$\frac{\partial \varphi}{\partial t} = \frac{2\pi}{\Phi_0} V . \quad (2.6)$$

The first of the two above-mentioned operating modes describes the zero-voltage state, i.e. $I < I_c$ (zero-voltage state). Here, the entire injected current is carried by Cooper pairs, so $I = I_s = \text{const}$. As a result, φ is constant over time, which, according to equation (2.6), leads to $V = 0$. This is known as the *dc Josephson effect*.

For $I > I_c$ however, Cooper pairs begin to break up such that a portion of the current needs to be carried by quasiparticles, which will then lead to a voltage drop V . According to the second Josephson equation, the phase φ becomes time dependent, and after integration one obtains

$$\varphi = \frac{2\pi}{\Phi_0} V t + \varphi_0 = w_J t + \varphi_0 \quad \text{with} \quad w_J = \frac{2\pi}{\Phi_0} V . \quad (2.7)$$

Thus, if we insert equation (2.7) into equation (2.3), we observe that the current I_s oscillates with the *Josephson frequency* $\frac{f_J}{V} = \frac{w_J}{2\pi V} = \frac{1}{\Phi_0} \approx 483.6 \text{ MHz}/\mu\text{V}$. Accordingly, this phenomenon is referred to as the *ac Josephson effect*.

2.1.2 Josephson Junctions in a Magnetic Field

To motivate the structure of a dc-SQUID, it is essential to first investigate the current behavior of an extended Josephson junction in the presence of an external magnetic field. So far, all previous formulae apply for point-like junctions, assuming a spatially constant phase difference φ and Josephson current density J_s across the junction area. This is not the case for three-dimensional (extended) junctions with a length L and width W . The *Josephson penetration depth* λ_J is a quantity used to classify an extended junction as short ($W, L \leq \lambda_J$) or long ($W, L \geq \lambda_J$) and is defined as

$$\lambda_J = \sqrt{\frac{\Phi_0}{2\pi\mu_0 J_{\text{c}} t_B}} . \quad (2.8)$$

Here, the magnetic thickness is defined as $t_B = d + \lambda_{L,1} + \lambda_{L,2}$, where d is the geometric thickness of the isolator. It describes how far an external magnetic field penetrates

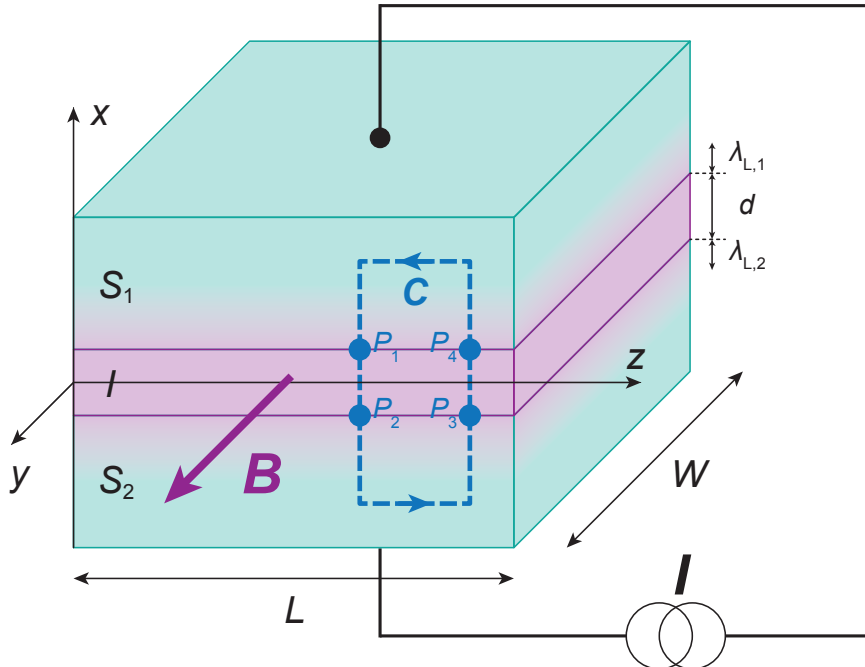


Figure 2.3: Short Josephson junction connected to a current source in the presence of an external B -field in y -direction, parallel to the junction area. Inside the electrodes the magnetic field decays exponentially according to the London penetration depths $\lambda_{L,1}$ and $\lambda_{L,2}$, visually shown by the purple color gradient. The closed contour C is used to derive expressions for the spatially dependent phase difference φ and current density J_s .

both superconducting electrodes if applied parallel to the junction area, as depicted in figure 2.3. The respective London penetration depths are $\lambda_{L,1}$ and $\lambda_{L,2}$ and $J_c = \frac{I_c}{WL}$ is the critical current density. This distinction is needed to determine whether the magnetic self-field generated by the supercurrent is negligible in comparison to the external field (short junctions) or not (long junctions). Within the scope of this thesis, we only use short junctions.

To analyze the current and phase distribution of such a junction we consider the setup shown in figure 2.3. A short junction is connected to a current source and is penetrated by an external B-field in y-direction, parallel to the junction area. Now, obtaining an expression for the phase requires a similar approach as the calculation for the quantized flux, where we assumed that the phase changes by $2\pi n$ around a closed loop. Here, we again integrate over a closed contour C , with the points $P_1 - P_4$ marking the transitions between superconductor and isolator. Using equation 2.5, we find

$$\frac{\partial\varphi}{\partial z} = \frac{2\pi}{\Phi_0} B_y t_B \quad \text{and} \quad \frac{\partial\varphi}{\partial y} = -\frac{2\pi}{\Phi_0} B_z t_B . \quad (2.9)$$

In this experiment, however, the magnetic field points in y-direction only, meaning φ will only vary along the z-axis. Integrating the first expression in equation 2.9 then leads to

$$\varphi(z) = \frac{2\pi}{\Phi_0} B_y t_B z + \varphi_0 . \quad (2.10)$$

Here, the integration constant φ_0 represents the phase difference for the case $z = 0$. Inserting equation 2.10 into the first Josephson equation and using $J_s = \frac{I_s}{WL}$ gives

$$J_s(y, z, t) = J_c(y, z) \sin(kz + \varphi_0) \quad \text{with} \quad k = \frac{2\pi}{\Phi_0} B_y t_B . \quad (2.11)$$

If we now assume the critical current density J_c to be constant across the junction area, we can integrate equation 2.11 to get a flux-dependent maximum Josephson current

$$I_s^m(\Phi) = I_c \left| \frac{\sin\left(\frac{kL}{2}\right)}{\frac{kL}{2}} \right| = I_c \left| \frac{\sin\left(\frac{\pi\Phi}{\Phi_0}\right)}{\frac{\pi\Phi}{\Phi_0}} \right| , \quad (2.12)$$

where $\Phi = B_y t_B L$ is the total flux threading through the junction. This expression describes the so-called Fraunhofer diffraction pattern, shown in figure 2.4. The result resembles the single slit experiment, where the same pattern is found for the light

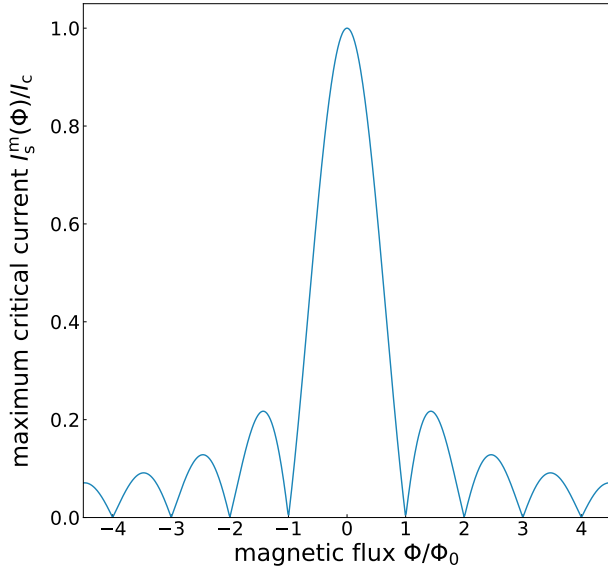


Figure 2.4: Normalized flux-dependent maximum Josephson current $I_s^m(\Phi)$ showing a Fraunhofer pattern. It modulates with the flux quantum Φ_0 , peaking at $\Phi = 0$ with subsequent maxima at $\Phi = \pm(\frac{3}{2} + n)\Phi_0$ with $n \in \mathbb{N}_0$. For $\Phi = \pm(n + 1)\Phi_0$ the total net current is zero.

intensity behind the slit. Here, the analogy works by considering the integral of the critical current density J_c as a transmission function which is constant inside the junction and zero outside.

2.1.3 RCSJ Model

The Fraunhofer pattern describes the flux-dependent current for the case of $I < I_c$, staying in the so-called zero-voltage state. In this regime, only the dc Josephson effect applies as discussed in subsection 2.1.1. Switching to the voltage stage, i.e. $I > I_c$, Cooper pairs start breaking up into quasiparticles if the electric energy eV exceeds the sum of both electrodes' gap energies $\Delta_1(T) + \Delta_2(T)$ [Bar57]. Consequently, at the *gap-voltage*

$$V_g = \frac{\Delta_1(T) + \Delta_2(T)}{e} \quad (2.13)$$

quasiparticles start to cross the tunnel barrier resulting in a steep rise of a resistive normal current I_n . This process also occurs at finite temperatures for $k_B T > \Delta_1(T) + \Delta_2(T)$, leading to a reduction of I_c as well as V_g . Under a dc current source, the condition $I = I_s + I_n$ must be constantly fulfilled. This results in an oscillating normal current and therefore voltage, since I_s oscillates with f_J according to the ac Josephson effect. According to the second Josephson equation (2.6) the oscillating voltage thus causes the term $\frac{d\varphi}{dt}$ to vary sinusoidally, causing both I_s and I_n and

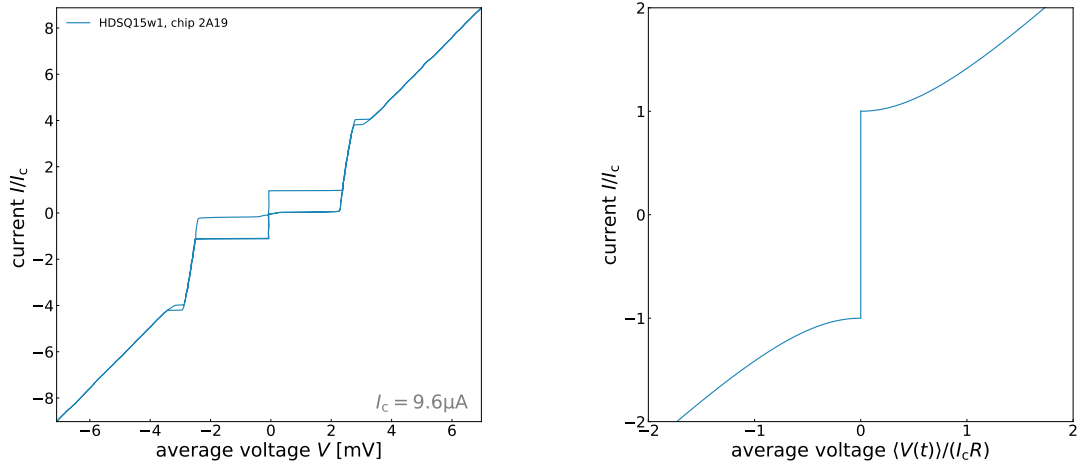


Figure 2.5: Left: Measured IVC of an underdamped junction manufactured in this working group, showing the typical hysteresis. Right: Theoretical IVC of an overdamped junction with a current-voltage shape that is independent of the current sweep direction.

in turn the resulting voltage to oscillate in a complex manner. As a voltage with such a high frequency cannot be measured, only the time-averaged voltage will be considered in the following discussion.

Now, further increasing the energy of the quasiparticles ($T > T_c$ and/or $V > V_g$) leads to a transition into normal-conducting electrons, which exhibit an ohmic dependence. This behavior can be seen in the typical current-voltage-characteristic (IVC) depicted in figure 2.5.

For real junctions, however, one needs to take into account that they are comprised of two electrodes separated by a thin insulating layer, which represent a parallel plate capacitor with the Al-AlO_x layer being the dielectric material. Therefore, a junction capacitance C needs to be taken into account. A displacement current I_d will flow as a consequence, given we are in the voltage state. Lastly, thermal and 1/f noise cause a small fluctuating current I_f . All these current channels were defined in the so-called Resistively and Capacitively Shunted Junction (RCSJ) model [McC68], [Ste68], which models the total current of a lumped (0-dimensional) junction to a sufficiently high accuracy. A schematic of an effective circuit diagram is shown in figure 2.6 (left). Combining every current channel leads to the *Basic Junction Equation*, which is defined as [Gro16]

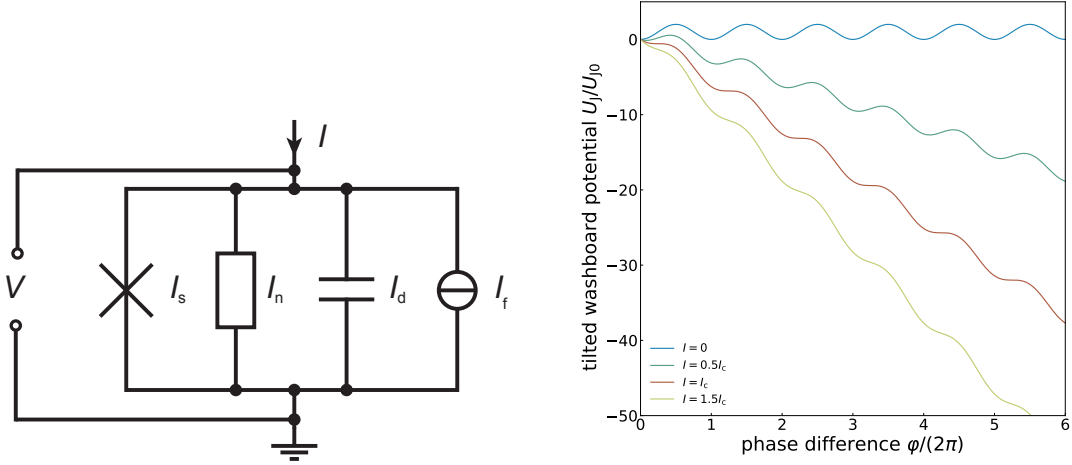


Figure 2.6: Left: Schematic circuit of a lumped Josephson junction with all four current channels connected in parallel, according to the RCSJ model. The junction is represented by the cross symbol on the left, marking the supercurrent I_s . The normal current I_n is realized with a resistance R , while the displacement current I_d and the noise I_f are attributed to a capacitor C and a current source, respectively. Right: Tilted washboard potential for different currents, ranging from 0 to $1.5I_c$. The tilt increases with the injected current I .

$$I = I_s + I_n + I_d + I_f = I_c \sin(\varphi) + \frac{1}{R(V)} \frac{\Phi_0}{2\pi} \frac{d\varphi}{dt} + C \frac{\Phi_0}{2\pi} \frac{d^2\varphi}{dt^2} + I_f . \quad (2.14)$$

By defining the Josephson coupling energy $U_{j0} = \frac{\hbar I_c}{2e}$ and the normalized currents $i = \frac{I}{I_c}$ and $i_f(t) = \frac{I_f(t)}{I_c}$, equation 2.14 can be rewritten to

$$\left(\frac{\hbar}{2e}\right)^2 C \frac{d^2\varphi}{dt^2} + \left(\frac{\hbar}{2e}\right)^2 \frac{1}{R(V)} \frac{d\varphi}{dt} + \frac{d}{d\varphi} \{U_{j0} [1 - \cos \varphi - i\varphi + i_f(t)\varphi]\} = 0 . \quad (2.15)$$

The expression in the curly brackets represents the potential energy in the system U_J , allowing equation 2.14 to be compared to

$$M \frac{d^2x}{dt^2} + \eta \frac{dx}{dt} + \nabla U = 0 , \quad (2.16)$$

which describes a particle with mass M and damping η moving inside the potential U . This mechanical analogue therefore allows us to interpret a *phase particle*, where

it's motion corresponds to a change of the gauge-invariant phase difference φ within a potential U_J [Cla04]. Consequently, it is attributed with a mass $M = \left(\frac{\hbar}{2e}\right)^2 C$ and damping $\eta = \left(\frac{\hbar}{2e}\right)^2 \frac{1}{R(V)}$. Figure 2.6 (right) visualizes how this phase particle behaves for different currents I . Given the shape of $U_J(\varphi)$, the potential is referred to as the *tilted washboard potential*.

For $I = 0$, the phase particle will remain within one of the potential minima. As the current increases, however, the potential starts to tilt such that the depth of the minima reduces until it vanishes for $I = I_c$, thus becoming a saddle point. Up until this point, the phase particle can't overcome the potential barrier to move downward, which agrees with the second Josephson equation as the phase difference φ should remain constant on average for $I < I_c$. Further increasing the current and therefore the tilt of the potential causes the phase particle to fall along the potential, resulting in a voltage drop across the junction ($\frac{\partial\varphi}{\partial t} > 0$).

Reversing the current sweep showcases the importance of the particle's mass M and damping η , as they determine if the return path equals the current shape described above or not. For the case of a small mass (small C) and large damping (small R), the phase particle will, due to a lack of momentum, come to a halt as soon as minima reappear in the washboard potential by reducing the current below I_c . The current path will therefore remain unchanged as I is reduced back to 0, as shown in figure 2.5 (right). Such a junction is consequently called an *overdamped* junction.

The other case describes an *underdamped* junction (figure 2.5 (left)) and involves a large mass (large C) and small damping (large R). This allows the phase particle to continue to move downward as it now carries enough momentum to overcome the arising maxima and minima. The finite voltage drop despite the current being below I_c is displayed as the steep quasiparticle current curve, which ends with a return current I_R that arises with the recapture of the particle in a minimum. This leads to a hysteretic IVC, as depicted in figure 2.5 (left). I_R can be calculated via [Lik86]

$$I_R = \frac{4}{\pi\sqrt{\beta_C}} I_c , \quad (2.17)$$

with β_C being the dimensionless Stewart-McCumber parameter, that is used to quantitatively distinguish between both junction types. It is given by

$$\beta_C = \frac{2\pi}{\Phi_0} I_c R^2 C \quad (2.18)$$

with $\beta_C \gg 1$ corresponding to a strongly underdamped junction, whereas $\beta_C \ll 1$ represents a strongly overdamped junction. The junctions developed and produced within the scope of this thesis aim to be overdamped, which is why we take a closer

look on the time-averaged voltage for $I > I_c$ in the case of $\beta_C \ll 1$. Neglecting the noise in equation 2.15, as well as assuming the resistance to be linear below and above the gap voltage V_g , i.e. $R(V) = R$, the time-averaged voltage can be derived to [Cla04]

$$\langle V(t) \rangle = I_c R \sqrt{\left(\frac{I}{I_c}\right)^2 - 1} \quad \text{for} \quad \frac{I}{I_c} > 1 . \quad (2.19)$$

This equation will be crucial to determine the voltage drop of a dc-SQUID, as its derivation is analogous to that of a single junction, which will be covered in the next section.

2.2 dc-SQUIDS

We have now covered the theoretical framework necessary to understand the working principle of a dc-SQUID, which consists of a superconducting ring intersected by two identical Josephson junctions with critical Josephson currents I_c , as depicted in figure 2.7. Both junctions are shunted with shunt resistors R_s to avoid hysteretic behavior in the respective IVCs. If the loop is then biased with a bias current I_b while being threaded by an external magnetic flux Φ_e , it is possible to convert small flux variations into a measurable voltage change. dc-SQUIDs are therefore used as highly sensitive flux-to-voltage transducers.

2.2.1 Zero Voltage State

In order to fully understand the working principle of a dc-SQUID it is again necessary to first cover the zero voltage stage as we did for a single junction. The parallel connection of the two junctions allows the bias current to split into two supercurrents I_{s1}, I_{s2} with identical critical currents, i.e. $I_{c,1} = I_{c,2} = I_c$. Here we assume $I_b < 2I_c$ to ensure that no voltage drop across both junctions occurs ($V_s = 0$). Applying Kirchhoff's law we then obtain the following expression

$$I_b = I_s = I_c \sin \varphi_1 + I_c \sin \varphi_2 = 2I_c \cos\left(\frac{\varphi_1 - \varphi_2}{2}\right) \sin\left(\frac{\varphi_1 + \varphi_2}{2}\right) . \quad (2.20)$$

In chapter 2.1.2 we concluded that a magnetic flux Φ causes the supercurrent to modulate with Φ_0 . A dc-SQUID can be considered as a single junction with a much larger effective area A_{eff} (loop area), that an external magnetic flux can penetrate. It is therefore reasonable to expect a similar behavior for a dc-SQUID. The same approach as with a single junction is used to determine the flux dependence of the

total supercurrent, where a closed loop integral is performed around the SQUID loop. The calculation leads to the relation [Gro16]

$$\varphi_2 - \varphi_1 = \frac{2\pi\Phi}{\Phi_0} , \quad (2.21)$$

which can be directly inserted into equation 2.20 to obtain

$$I_s = 2I_c \cos\left(\pi \frac{\Phi}{\Phi_0}\right) \sin\left(\varphi_1 + \pi \frac{\Phi}{\Phi_0}\right) . \quad (2.22)$$

In the most general case, however, one needs to take into account the inductance L_s of the SQUID loop and therefore a circulating current $I_{\text{cir}} = \frac{I_{s1}-I_{s2}}{2}$ that induces the additional flux $\Phi_{\text{cir}} = L_s I_{\text{cir}}$. With the external flux Φ_e we can thus write for the total flux

$$\Phi = \Phi_e + \Phi_{\text{cir}} \quad (2.23)$$

$$= \Phi_e - L_s I_c \sin\left(\pi \frac{\Phi}{\Phi_0}\right) \cos\left(\varphi_1 + \pi \frac{\Phi}{\Phi_0}\right) \quad (2.24)$$

$$= \Phi_e - \frac{1}{2} \beta_L \Phi_0 \sin\left(\pi \frac{\Phi}{\Phi_0}\right) \cos\left(\varphi_1 + \pi \frac{\Phi}{\Phi_0}\right) . \quad (2.25)$$

Here, we introduced the dimensionless screening parameter $\beta_L = \frac{2L_s I_c}{\Phi_0}$, which relates the maximum possible flux $\Phi_{\text{cir}}^{\max} = L_s I_{\text{cir}}^{\max} = L_s I_c$ produced by screening currents to $\frac{\Phi_0}{2}$. This quantity describes the influence the screening currents have on the total flux Φ , which in turn affects I_s in equation 2.22. We will now simplify the expression above by considering the limiting case for small currents, i.e. $I_s \ll 2I_c$.

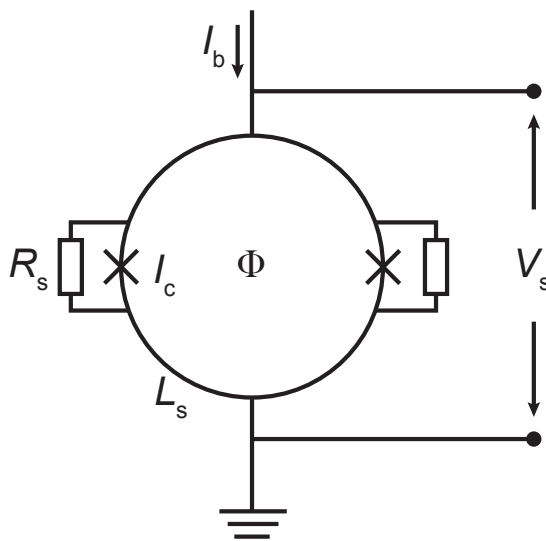


Figure 2.7: Schematic circuit diagram of a shunted dc-SQUID. A superconducting loop with inductance L_s is interrupted by two lumped Josephson junctions such that they form a parallel connection. Operation requires a bias current I_b and an external magnetic flux Φ . To avoid hysteresis effects, a shunt resistance R_s is connected to each junction.

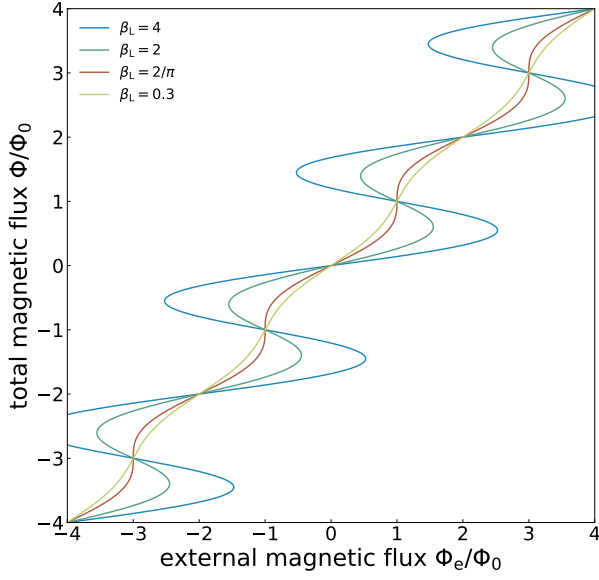


Figure 2.8: Normalized flux Φ modulated by the external flux Φ_e . The amplitude of the modulation depends on the screening parameter β_L , where $\Phi(\Phi_e)$ remains a single-valued function for $\beta_L \leq 2/\pi$.

This condition implies that $\sin \varphi_1 \approx -\sin \varphi_2$ and thus $\varphi_1 \approx -\varphi_2$, leading to a vanishing cosine argument $\varphi_1 + \pi \frac{\Phi}{\Phi_0} \approx 0$. This results in

$$\Phi = \Phi_e - \frac{1}{2}\beta_L\Phi_0 \sin\left(\pi \frac{\Phi}{\Phi_0}\right) . \quad (2.26)$$

Figure 2.8 showcases this relation for several values of β_L . High values ($\beta_L > 2/\pi$) correspond to hysteretic characteristics, meaning there can be multiple values of total flux Φ for the same applied flux Φ_e . For practical dc-SQUIDs, it is therefore desirable to avoid this ambiguous behavior. The intersections of each curve represent the case for $\Phi = n\Phi_0$, such that the screening currents vanish and the total flux equals the external flux ($\Phi = \Phi_e$). This is to be expected as the flux in a superconducting ring needs to be quantized (see equation 2.2). Consequently, the SQUID tries to maintain the total flux at integer values of Φ_0 for the limiting case of $\beta_L \gg 1$, where Φ_{cir} dominates over any applied flux. This compensation is visualized by the strong modulation for high β_L in figure 2.8, where a wide range of Φ_e values remain in the proximity of $n\Phi$. The other limiting case, i.e. $\beta_L \ll 1$, allows us to neglect the circulating currents such that we can write $\Phi \approx \Phi_e$. From equation 2.22 we then obtain the maximum possible supercurrent

$$I_s^m(\Phi_e) = 2I_c \left| \cos\left(\pi \frac{\Phi_e}{\Phi_0}\right) \right| . \quad (2.27)$$

The modulation of this current quickly diminishes for increasing β_L , as was derived

in [Cla04] to

$$\frac{\Delta I_s^m(\Phi_e)}{2I_c} \approx 1 - \frac{2\Phi_e}{\Phi_0\beta_L} . \quad (2.28)$$

For the SQUIDs produced within the scope of this thesis, values of $\beta_L \approx 1$ were considered optimal to minimize resonant behavior without reducing the SQUID inductance L_s too much. In subsection 2.2.3 we will discuss how various parameters are chosen to ensure an optimal SQUID performance.

2.2.2 Voltage State

To utilize dc-SQUIDs as sensitive magnetometers, it is necessary to operate them in the voltage state by applying a large enough current bias I_b , such that $I_b > 2I_c$. In the case of negligible screening ($\beta_L \ll 1, \Phi \approx \Phi_e$) and strong damping ($\beta_C \ll 1$), i.e. by choosing a small junction capacitance C and SQUID inductance L_s , it is possible to derive the flux dependence of the resulting voltage drop across the SQUID. Following the RCSJ model, we are only left with the supercurrent I_s and the resistive current I_n , such that by using equation 2.22 we can write for the bias current

$$I_b = 2I_c \cos\left(\pi \frac{\Phi_e}{\Phi_0}\right) \sin\left(\varphi_1 + \pi \frac{\Phi_e}{\Phi_0}\right) + 2 \frac{V_s}{R} , \quad (2.29)$$

where we again assumed identical junctions, each shunted by a small shunt resistor $R_s \ll R_n$. Here R_n denotes the normal resistance of a single, unshunted junction. Therefore the total normal resistance R for each parallel connection is approximately $R \approx R_s$. Additionally, we can define a new phase $\varphi = \varphi_1 + \pi \frac{\Phi}{\Phi_0}$ and with the maximum supercurrent from equation 2.27 we obtain a current relation that resembles that of a single junction:

$$I_b = I_s^m(\Phi_e) \sin(\varphi) + \frac{2}{R_s} \frac{\Phi_0}{2\pi} \frac{\partial \varphi}{\partial t} . \quad (2.30)$$

This equivalence of a dc-SQUID and a single junction stems from the above-mentioned fact that the SQUID loop represents a single Josephson contact that provides a larger effective area external fields can penetrate. It is therefore possible to derive the voltage drop across the SQUID in the same manner as in subsection 2.1.3. With the critical current $I_s^m(\Phi_e)$ now being flux-dependent with a modulation of Φ_0 , we can

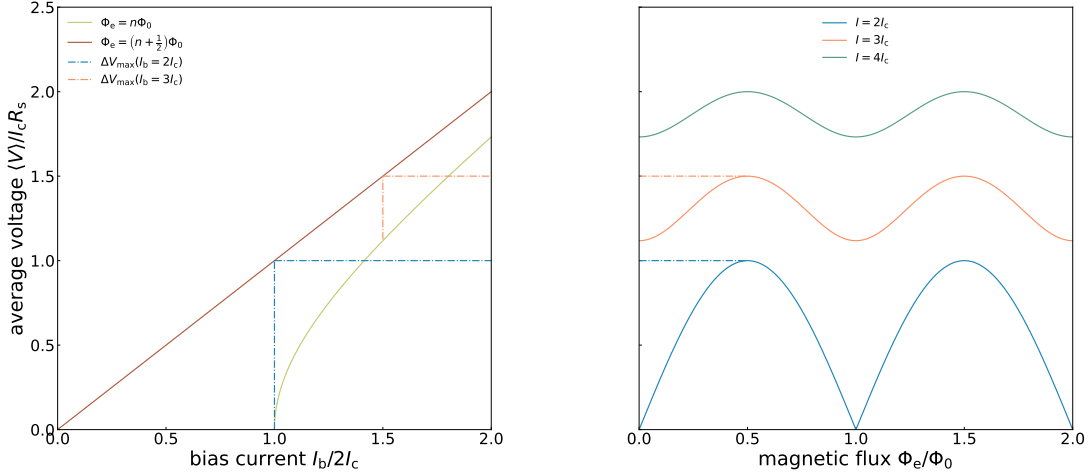


Figure 2.9: Left: IV-characteristics for the total flux $\Phi \approx \Phi_e$ being an integer and half integer number of flux quanta, given that $\beta_C \ll 1$ and $\beta_L \ll 1$. The maximum voltage swing ΔV_{max} is approximately at $I_b \approx 2I_c$ and corresponds to $I_c R_s$ for a resistively shunted dc-SQUID. Right: The projection of equation 2.31 onto the $V\Phi$ -plane shows the flux dependence of the voltage at the bias current values $I_b = 2I_c$, $I_b = 3I_c$ and $I_b = 4I_c$. The amplitude of the modulation decreases for increasing I_b .

compare to equation 2.19 and obtain for the time averaged voltage [Cla04]

$$\langle V(t) \rangle = \frac{R_s}{2} \sqrt{I_b^2 - I_s^m(\Phi_e)^2} \quad (2.31)$$

$$= I_c R_s \sqrt{\left(\frac{I_b}{2I_c}\right)^2 - \left[\cos\left(\pi \frac{\Phi_e}{\Phi_0}\right)\right]^2}. \quad (2.32)$$

Evidently, both the current and the voltage are flux dependent and are modulated by Φ_0 . Figure 2.9 (left) showcases this behavior by considering the case for the minimum and maximum critical current, i.e. for $\Phi_e = n\Phi_0$ and $\Phi_e = (n + \frac{1}{2})\Phi_0$, with $n \in \mathbb{Z}$. The current-voltage-characteristics at these flux values are particularly interesting, as they can be used to extract crucial SQUID parameters like the voltage swing ΔV_{max} . This property describes how the voltage varies with the applied flux Φ_e , at a given current I_b . It is maximal at $I_b \approx 2I_c$, as depicted in figure 2.9 (right).

It is, however, important to note that equation 2.31 doesn't hold for practical SQUIDS, as they are typically not fabricated to fulfill the limiting case of $\beta_C \ll 1$ and $\beta_L \ll 1$. The conclusions reached here will nevertheless be applicable to practical SQUIDS, only needing a few adjustments.

2.2.3 Optimal Parameters

Negligible screening is not reasonable, as it would require to choose an extremely small SQUID inductance L_s , which in turn deteriorates the sensitivity for magnetic fields. The main reason to construct a dc-SQUID was to obtain a highly sensitive magnetometer by creating a large area for magnetic fields to thread through. Also, the fabrication process doesn't allow to produce an arbitrarily small junction capacitance C . The parameter β_C will therefore reach a lower limit as well, since also decreasing R_s too much reduces the voltage swing ΔV_{\max} and increases the energy sensitivity $\epsilon(f)$, as we will see in subsection 2.2.4. Now by allowing displacement and fluctuation currents, the current and voltage expressions become analytically unsolvable and therefore have to be solved numerically. In [Tes77] such numerical simulations lead to optimal values of $\beta_C \approx 1$ and $\beta_L \approx 1$ to minimize the energy sensitivity.

To further fine-tune various parameters it is essential to look at how dc-SQUIDs are typically operated to achieve the highest possible flux sensitivity. Here, we distinguish between a current and a voltage bias, where the former was assumed in figure 2.9. Maximizing sensitivity in this mode is done by maintaining the flux thorough a constant offset at the steepest point in the $V\Phi$ -curve, which is referred to as the working point and corresponds to $\Phi_e = (2n + 1)\frac{\Phi_0}{4}$. This allows for the largest possible voltage change ΔV at a given flux change $\Delta\Phi$. Similarly, at a voltage bias the working point will mark the steepest point in the $I\Phi$ -curve. To quantify this, we introduce the transfer parameters

$$V_\Phi \equiv \left| \left(\frac{\partial V}{\partial \Phi_e} \right) \right| \quad (2.33)$$

$$I_\Phi \equiv \left| \left(\frac{\partial I}{\partial \Phi_e} \right) \right|. \quad (2.34)$$

As mentioned above, at $I_b \approx 2I_c$ (current bias) the amplitude of the voltage modulation is maximal. This needs to be modified for practical SQUIDS, where thermal fluctuations can't be neglected. The resulting thermal current I_{th} causes a rounding of the edge at $I_b = 2I_c$ (figure 2.9 (left)), thereby reducing ΔV_{\max} and V_Φ [Iva68]. To minimize this effect, numerical simulations were made that lead to the condition [Cla88]

$$\frac{I_c}{5} \geq I_{\text{th}} \equiv \frac{2\pi k_B T}{\Phi_0} . \quad (2.35)$$

A lower bound for I_c at $T = 4.2\text{ K}$ will therefore be approximately $1\text{ }\mu\text{A}$. This effect

shifts the current $I_{b,\max}$, at which the voltage swing is maximal, according to [Dru96b] by a temperature correction factor leading to

$$I_{b,\max} \approx 2I_c(1 - \sqrt{\Gamma/\pi}) \quad , \quad (2.36)$$

where Γ is the noise parameter defined as $\Gamma = I_{\text{th}}/I_c$. Lastly, the thermal current can also be used to set an upper limit to the SQUID inductance. We can define a thermal inductance $L_{\text{th}} = \frac{\Phi_0}{2I_{\text{th}}}$ for the thermal current inducing half a flux quantum. This should be significantly larger than the SQUID inductance L_s to minimize the impact of these thermal fluctuations. Again, simulations provide a constraint for optimization, giving the relation [Cla88]

$$5L_s \leq L_{\text{th}} \equiv \frac{\Phi_0}{2I_{\text{th}}} = \frac{\Phi_0^2}{4\pi k_B T} \quad . \quad (2.37)$$

For $T = 4.2\text{ K}$ we would obtain $L_s \leq 1\text{ nH}$, which is typically fulfilled for practical dc-SQUIDs.

2.2.4 Noise

The above-mentioned energy sensitivity, also called spectral noise energy density or energy resolution, is defined as the flux noise per SQUID inductance L_s and is typically expressed through a power spectral density as

$$\epsilon(f) = \frac{S_\Phi(f)}{2L_s} \quad . \quad (2.38)$$

This conveniently allows to compare noise properties from SQUIDs with different loop inductances. The flux noise power spectral density $S_\Phi(f)$ cannot be measured directly and is therefore calculated with the equivalent voltage noise using the transfer coefficient introduced above:

$$S_\Phi(f) = \frac{S_V(f)}{V_\Phi^2} \quad . \quad (2.39)$$

The flux noise in SQUIDs is typically separated into a high frequency constant white noise and a low frequency $1/f$ -noise component [Koc07]. To derive an expression for $S_V(f)$ we consider the white noise regime only, limiting ourselves to higher frequencies to avoid any significant influence of $1/f$ -noise. For this we need to distinguish between two noise currents, one flowing across the SQUID and the other circulating within the SQUID loop. The former sees the total resistance of the SQUID which corresponds

to $\frac{R_s}{2}$ for $I \gg I_{b,\max}$ and to the dynamic resistance $R_{\text{dyn}} = \frac{\partial V}{\partial I}$ for operation at the working point. The circulating current, however, sees two resistances in series, i.e. $2R_s$. By taking into account noise inducing resonances due to the simulated optimal values of $\beta_C \approx 1$ and $\beta_L \approx 1$ that exhibit hysteretic behavior, both noise currents can be used to obtain the voltage noise given by [Tes77], [Bru82]

$$S_V(f) = \frac{4k_B T}{R_s} \left[2R_{\text{dyn}}^2 + \frac{L_s^2 V_\Phi^2}{2} \right] . \quad (2.40)$$

Here, we used the approximation $V_\Phi \approx \frac{I_c R_s}{\Phi_0/2} \approx \frac{R_s}{L_s}$ for $\beta_L \approx 1$. These calculations also derived the relation $R_{\text{dyn}} \approx \sqrt{2}R_s$, which can be used to rewrite equation 2.40 to

$$S_V(f) = 18k_B T R_s . \quad (2.41)$$

Inserting this into equations 2.39 and 2.38 leads to the expression

$$\epsilon(f) \approx 16k_B T \sqrt{\frac{L_s C}{\beta_C}} \approx 16k_B T \sqrt{L_s C} \quad \text{for } \beta_C \approx 1 . \quad (2.42)$$

For a moderately damped dc-SQUID ($\beta_C \approx 1$) at a temperature $T = 100 \text{ mK}$ and with a suitably small inductance $L_s = 100 \text{ pH}$ we would therefore obtain a theoretical value of $\epsilon \approx 0.32 \text{ h}$.

Lastly, to get the full picture we will look at the total flux noise spectrum by considering the $1/f$ component. This not entirely understood noise behavior is added to the above derived white noise and dominates the low frequency regime. It is parameterized by a power density at 1 Hz, giving a total noise power density of

$$S_\Phi(f) = S_{\Phi,w} + \frac{S_{\Phi,1/\text{f}}(1 \text{ Hz})}{f^\alpha} , \quad (2.43)$$

with $S_{\Phi,w}$ being the white noise component and α ranging between 0.5 and 1 [Dru11], which can be determined through experiment.

2.2.5 Parasitic Resonances

We have seen that optimizing dc-SQUID properties requires careful fine-tuning of various parameters to ensure high sensitivity and low noise at the same time. Another constraint in this regard involves the presence of resonances in the system that we need to take into account. As discussed in subsection 2.1.3, a Josephson contact

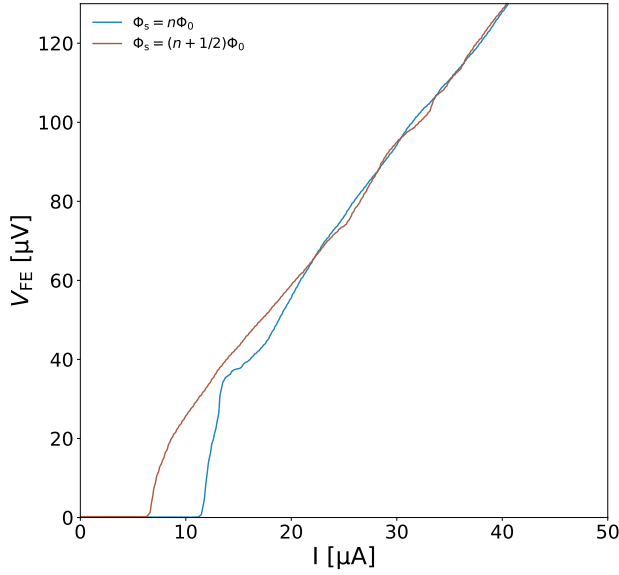


Figure 2.10: Measured IV-characteristic of a dc-SQUID developed within the scope of this thesis. The first current step at $V_s \approx 40 \mu\text{V}$ corresponds to the fundamental SQUID resonance for $L_s = 119 \text{ pH}$ and $C = 0.95 \text{ pF}$.

represents a parallel plate capacitor with capacitance C . Due to the series connection of the two junctions within the SQUID loop, we obtain a total capacitance of $C/2$. The SQUID with its loop inductance L_s will therefore form an LC resonator that can be excited if the Josephson currents oscillate with the resonance frequency $f_{L_sC} = \frac{1}{2\pi\sqrt{L_sC/2}}$. This is fulfilled for the condition

$$\frac{V_s}{\Phi_0} = \frac{1}{2\pi\sqrt{L_sC/2}} , \quad (2.44)$$

where V_s denotes the voltage drop across the SQUID that is associated with the Josephson frequency $f_J = \frac{V_s}{\Phi_0}$ resulting from the ac Josephson effect. With optimal β_C and β_L values the voltage corresponding to this resonance frequency will move towards the vicinity of the working point, thus becoming relevant for the SQUID's performance. This so-called *fundamental SQUID resonance* negatively affects the operation range by manifesting itself through a current step in the IVC, as shown in figure 2.10. The IV curves for integer and half integer flux quanta intersect as a result multiple times, due to higher harmonics of the resonance causing additional current steps [Cla04]. The voltage swing ΔV and consequently V_Φ are therefore limited by this resonance, which favors the choice of small values for L_s and C .

It is important to note, that the fundamental resonance does not depend on any geometrical structures of the circuit, which typically play a significant role in practical SQUIDs. Resonance inducing structures are however necessary for practical reasons.

Those include the need for effectively coupling external flux changes into the SQUID in order to take advantage of its high sensitivity. For this an external input coil with inductance L_i is usually fabricated on top of the SQUID loop, separated by an insulating layer to ensure the coupling to be solely inductive (see section 3.1). The SQUID can therefore be used as a current sensor by converting small current signals in the input coil into small magnetic flux changes in the SQUID. This added coil, however, provides another parasitic capacitance C_p resulting from its fabrication on top of the SQUID loop. Consequently, rf currents can couple inductively from one system into the other, causing further parasitic effects. Particularly, problematic LC resonances arise from the added inductance L_i and capacitance C_p , namely the $f_{L_s C_p}$ and $f_{L_i C_p}$ resonance. The latter can be excited for $f_J = f_{L_i C_p}$, since the Josephson currents are able to couple into the input coil. The parasitic capacitance C_p and consequently both resonance frequencies depend on geometrical factors such as the length of the input coil, as well as the widths and heights of the individual components that form the resonator. It has been shown, that these resonances lead to the energy sensitivity increasing proportional to $\sqrt{1 + 2C_p/C}$, as long as $C_p/C \leq 2$. For $C_p/C \geq 2$ the energy sensitivity saturates due to the resonance frequencies falling below the working point [Ryh92]. It is therefore desirable to minimize C_p as much as possible in order to reduce the resulting voltage noise.

The fabrication of the input coil on top of the SQUID loop also represents a microstrip transmission line, consisting of a conductor carrying the signal (input coil) and a ground plane (SQUID loop), separated by a dielectric layer. This forms a waveguide allowing electromagnetic waves to propagate alongside it, which undergo reflections where impedance mismatches occur. These would arise whenever the input coil exits the SQUID loop, thereby leaving the underlying ground plane. Standing waves occur if the length l of the signal carrying line above the ground plane corresponds to an integer number of half the wavelength of the Josephson frequency. This is consequently also called the $\lambda/2$ resonance. The corresponding resonance frequency

$$f_l = \frac{mc_{\text{str}}}{2l} , \quad (2.45)$$

where $m \in \mathbb{Z}$, depends on l and the material-dependent wave propagation velocity c_{str} . This resonance behavior also emerges if we consider the SQUID loop to be the signal carrying line with the input coil acting as the corresponding ground plane. Here it is again possible to move the resonance further away from the operation frequency at the working point by choosing adequate geometric proportions, e.g. by varying the length of the input coil or the SQUID loop. These methods to mitigate the influence of resonances can be complemented by direct damping through attenuators, which will be discussed in section 4.2. In chapter 4 we will cover how

various parameters are chosen in the SQUID design to suppress and avoid possible resonances, given the constraints we derived in subsection 2.2.3 and 2.2.4.

3. Experimental Methods

So far we discussed general aspects of dc-SQUIDs and how their working principle allows for highly sensitive measurements of magnetic flux changes. As already briefly seen in subsection 2.2.5, when it comes to practical SQUIDs many theoretical considerations regarding parameter optimization need to be reevaluated to account for usability in practical experiments. We begin this chapter with general concepts of a practical SQUID design and introduce a typical low-noise setup with a room temperature readout electronics. In this working group, SQUIDs are mainly developed for the readout of *Metallic Magnetic Calorimeters (MMCs)* (see section 3.3). We will see in the following how those SQUIDs need to be designed to optimize their coupling to these detectors.

3.1 Practical dc-SQUIDs

The SQUIDs developed in this working group are primarily used as current sensors for the MMC readout by coupling the detected signals from the *pickup coil* of the MMC to the parallel input coil of the SQUID. The need for this input coil entails a parasitic capacitance resulting in several resonances, as discussed in subsection 2.2.5. To achieve high inductive coupling between input coil and SQUID loop with inductances L_i and L_s , respectively, it is necessary to fabricate them closely on top of each other, only separated by a thin insulating layer. The coupling strength is given by the dimensionless parameter

$$k_{is} = \frac{M_{is}}{\sqrt{L_i L_s}} \quad , \quad (3.1)$$

where $M_{is} = \Delta\Phi_s / \Delta I_i$ is the mutual inductance, describing how much flux $\Delta\Phi_s$ is generated in the SQUID loop for a current change ΔI_i in the input coil. This allows us to define the so-called coupled energy sensitivity $\epsilon_c(f)$ with respect to the input coil, which by using equation 2.38 is given as

$$\epsilon_c(f) = \frac{\epsilon(f)}{k_{is}^2} = \frac{L_i S_{I,i}}{2} \quad . \quad (3.2)$$

This expression refers to the apparent current noise $S_{I,i} = S_{\Phi_s} / M_{is}^2$, which is generated by the flux noise from the SQUID loop through the coupling M_{is} . A strong

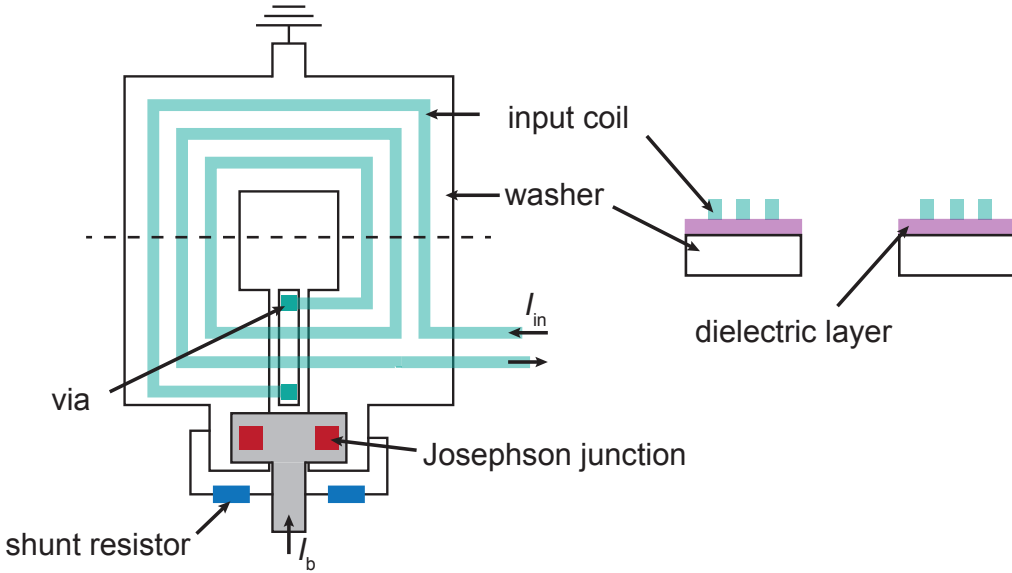


Figure 3.1: Schematic drawing of a typical planar thin-film dc-SQUID. The SQUID loop is realized as a square *washer*-geometry interrupted by a narrow slit, only connected at the junction area. A thin insulating layer separates the washer from the planar multi-turn input coil above. Left: View from the top. Right: Cross section marked by the dashed line.

coupling can be achieved by the commonly used square *washer*-geometry with a planar input coil [Jay81], as shown in figure 3.1.

Here, the SQUID loop is represented by the washer, whereas each turn of the input coil is located on top of it to maximize the coupling between both coils. A cross section of this setup is depicted in figure 3.1 (right), showing the insulating dielectric layer separating each coil. The washer is intersected by a slit, which starts at the square hole in the middle and ends at the remotely situated junction area that connects each side of the loop. The total inductance of the SQUID loop can be calculated by adding the dominating washer hole inductance L_h , the slit inductance $L_{sl} \approx 0.3 \text{ pH}/\mu\text{m}$ given for small slit dimensions and the much smaller parasitic inductance L_j associated with the junction area, giving [Ket91]

$$L_s = L_h + L_{sl} + L_j . \quad (3.3)$$

The latter is referred to as parasitic due to its position outside of the input coil, thus not contributing to the coupling. By neglecting L_{sl} and L_j , we can approximate the washer inductance in the limit of $d \ll w$ to $L_s \approx L_h \approx 1.25\mu_0 d$, where d and w are the inner and outer side lengths, respectively [Jay81]. This is a reasonable result considering that the supercurrent will only flow along the inner edge of the washer

[Ket82], thereby being independent of the outer side length w . The effective area A_{eff} of the SQUID loop has been calculated to $A_{\text{eff}} \approx dw$ [Ket85], showing that this geometry allows for high sensitivity while keeping the SQUID inductance small. The input coil inductance on the other hand can be approximated by $L_i = L_{\text{str}} + n^2 L_s$, where L_{str} is the stripline inductance (see section 5.2) and n is the number of input coil turns [Jay81]. The dc-SQUID designs used in this working group, however, are too complex to provide such analytical expressions and therefore need to be calculated numerically using simulation softwares such as *InductEX*¹.

3.1.1 Gradiometer

The high flux sensitivity of a SQUID makes it prone to detect unwanted magnetic bias fields and/or gradients that may be present during its operation. Typical SQUIDs are therefore built in a gradiometric design to counteract this effect [Ket78]. A first order gradiometer consists of two identical conducting loops connected in series or parallel, with opposing orientation as shown in figure 3.2 (left, middle). Under the presence of a homogeneous bias field \mathbf{B} in x -direction (perpendicular to the gradiometer plane), this configuration produces a zero net current after a field change ΔB_x , due to the opposing currents induced in each turn. To also achieve the same effect for a field gradient $\frac{\partial \mathbf{B}}{\partial z}$ or $\frac{\partial \mathbf{B}}{\partial y}$, a second order gradiometer composed of four loops in series or parallel is required, see figure 3.2 (right), where only the currents induced in the upper loops are drawn for the sake of overview. In order to incorporate this into a practical SQUID, the input coil and the SQUID loop will consist of four serial and parallel turns, respectively. This configuration enables to combine a small SQUID inductance with a large input coil inductance while maintaining a strong coupling between the two, as each turn of both coils can be produced with similar dimensions. The low SQUID inductance results from the reciprocal summation over each loop inductance L_l due to the parallel connection, giving

$$L_s = \frac{L_l}{4} . \quad (3.4)$$

Whereas a serial gradiometer gives

$$L_i = 4L_l \quad (3.5)$$

for the input coil. This gradiometric setup allows for adapting the input coil to the pickup coil of an MMC by choosing a large enough inductance L_i , which will be discussed in chapter 4.

¹SUNMagnetics, 15 De Beer Rd, Stellenbosch Central, Stellenbosch, 7600, South Africa

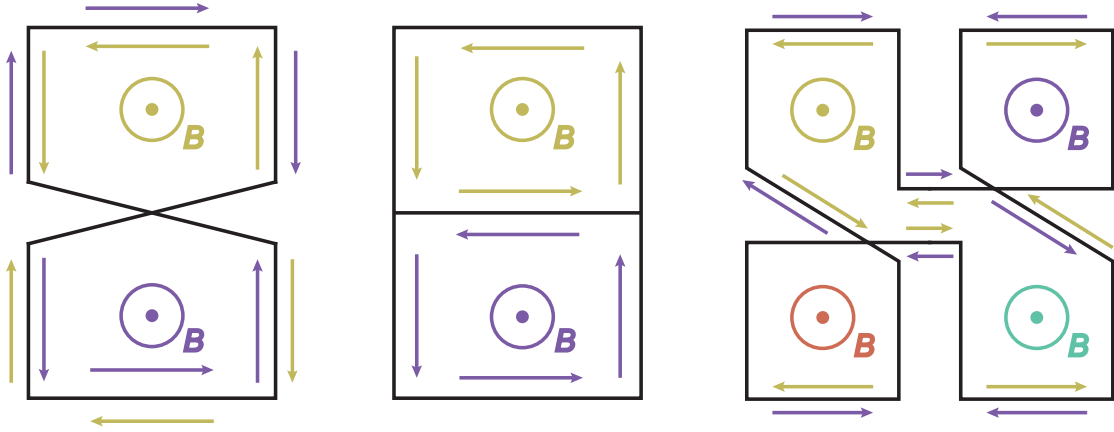


Figure 3.2: Schematic examples of a gradiometric dc-SQUID configuration threaded by a homogeneous magnetic field \mathbf{B} . A first order gradiometer can be realized by either connecting two loops in series (left) or in parallel (middle). A magnetic field change ΔB_x induces two opposing currents that cancel each other out. Right: Second order gradiometer consisting of four loops connected in series. This geometry results in a net zero current also for an applied field gradient $\frac{\partial \mathbf{B}}{\partial z}$. For the sake of clarity, the currents induced in the two bottom loops are omitted.

3.2 Operation of a dc-SQUID

The SQUIDs developed within the scope of this thesis are produced in the institute's cleanroom and then tested both in a single- and a two-stage setup (see subsection 3.2.2). The measurements described in chapter 5 are carried out at either $T = 4.2\text{ K}$ in a liquid helium transport vessel or in a dilution cryostat BF-LD250 from BlueFors² with a base temperature of $T = 10\text{ mK}$. The former submerges the SQUIDs in liquid helium via a dipstick, which provides a sample holder for PCBs. The SQUIDs are glued onto those PCBs and are electrically connected to them via aluminum bond wires, by utilizing the bond pads shown in figure 4.4. The sample holder is equipped with both a superconducting (niobium) and a soft-magnetic Cryoperm shield to suppress external magnetic fields. The read-out is done by a broadband SQUID electronics of the type XXF-1 (see subsection 3.2.1) to both supply the necessary bias and ramp current signals to the SQUID as well to provide the FLL feedback. The SQUID electronics is controlled via software and the voltage output observed on a Keysight InfiniiVision³ oscilloscope.

²BlueFors Cryogenics Oy, Arinatie, 00370 Helsinki, Finnland

³Keysight Technologies Deutschland GmbH, Herrenberger Straße 130, 71034 Böblingen

3.2.1 Flux-Locked Loop

We have seen in section 2.2.2 that the periodic $V\Phi$ -characteristic provides an approximately linear dependence at $\Phi = (2n + 1)\frac{\Phi_0}{4}$, which only holds for $\Delta\Phi \approx \Phi_0/4$. This restricts the dynamic range greatly, as the linearity vanishes for larger flux changes and for $\Delta\Phi > \Phi_0/2$ the voltage even becomes ambiguous. Such behavior is unsuitable for MMC readout, as they require the highest possible signal to noise ratio and therefore a linearized output voltage.

The standard readout method involves a flux feedback circuit to maintain the operation at the working point independently of the flux change amplitude [Dru02]. This so-called flux-locked loop (FLL) readout technique first amplifies the output signal of the SQUID V_s with a differential amplifier operated at room temperature, where the voltage V_b corresponding to the working point is provided by a voltage source on the second amplifier input. This voltage compensation at the working point ensures that only variations $\Delta V = V_s - V_b$ that correspond to the flux change $\Delta\Phi$ are amplified. The signal is then fed into an integrator, which integrates it over time and thus creates a rising output voltage V_{out} . By now connecting a feedback resistance R_{fb} to the output circuit, a rising feedback current I_{fb} emerges that flows to a feedback coil with inductance L_{fb} . This coil is coupled to the SQUID analogous to the input coil (see chapter 4), but with the opposite orientation. A compensation flux $-\Delta\Phi$ is generated up until the initial flux change is fully canceled out, i.e. $V_s \rightarrow 0$. The integrator will therefore approach a constant value due to the vanishing voltage at the input circuit. This voltage signal is proportional to the current that was needed to completely compensate for the input signal that induced $\Delta\Phi$, leading to the relation

$$V_{\text{out}} = \frac{R_{\text{fb}}}{M_{\text{fb}}} \Delta\Phi . \quad (3.6)$$

A schematic for this readout process is shown in figure 3.3. With this setup the SQUID is used as a null-detector that allows for the linearization of the quantity of interest, while also providing a large dynamic range. A state-of-the-art, low-noise SQUID readout electronic by the company Magnicon⁴ of the type XXF-1, which is used in this working group, provides the necessary current and voltage sources, as well as the room temperature amplifiers within the FLL circuit described above. This SQUID electronics exhibits an intrinsic voltage noise of $\sqrt{S_{V,\text{el}}} \approx 0.33 \text{ nV}/\sqrt{\text{Hz}}$ and intrinsic current noise of $\sqrt{S_{I,\text{el}}} \approx 2.6 \text{ pA}/\sqrt{\text{Hz}}$ [Dru06]. The included current source for the feedback coil couples current noise into the SQUID. In the work of [Kaa20], this contribution was determined to $\sqrt{S_{I,\Phi}} = 2.4 \text{ pA}/\sqrt{\text{Hz}}$ for the white noise and $\sqrt{S_{I,\Phi}} = 10 \text{ pA}/\sqrt{\text{Hz}}$ for the $1/f$ component at 1 Hz. Furthermore, a large amplifier

⁴Magnicon GmbH, Barkhausenweg 11, 22339 Hamburg

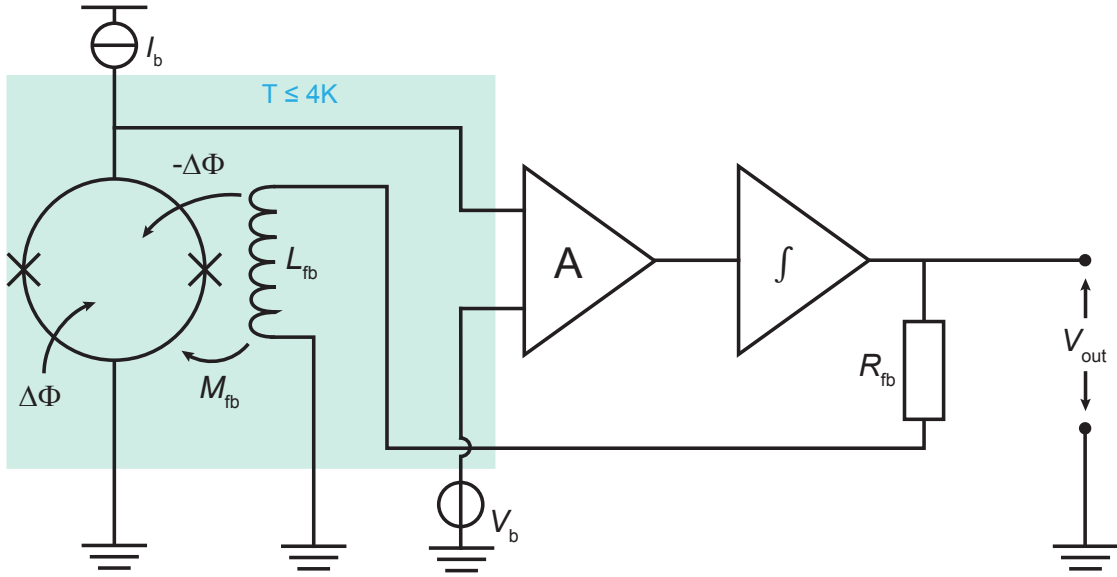


Figure 3.3: Schematic circuit diagram of a flux-locked loop dc-SQUID readout. The amplified and integrated SQUID voltage signal V_s , which is caused by a detected flux change $\Delta\Phi$, is fed back to a feedback coil with inductance L_{fb} , creating a compensating flux $-\Delta\Phi$. This enables the operation at the working point, while flux changes far greater than $\Phi_0/4$ can be linearized.

bandwidth of 6 MHz is provided to ensure high sensitivity for short signal rise times. The intrinsic noise of the SQUIDs produced in this working group, however, typically reaches values of $\sqrt{S_{\Phi_s}} \leq 1 \mu\Phi_0/\sqrt{\text{Hz}}$. Adding these terms together leads to the total apparent flux noise in the SQUID, which is expressed as the spectral power density

$$S_{\Phi_s, \text{SQ}} = S_{\Phi_s} + \frac{S_{V,\text{el}}}{V_{\Phi_s}^2} + \frac{S_{I,\text{el}}}{I_{\Phi_s}^2} + S_{I,\Phi} M_{fb}^2 . \quad (3.7)$$

Typical values for the transfer coefficients of SQUIDs produced within the scope of this thesis, are $V_{\Phi_s} = 80 \mu\text{V}/\Phi_0$ and $I_{\Phi_s} = 20 \mu\text{A}/\Phi_0$, leading to the SQUID electronics having a total noise contribution of $4.13 \mu\Phi_0/\sqrt{\text{Hz}}$. The amplifier noise therefore dominates the noise level, thereby deteriorating the signal to noise ratio. To avoid this effect, a second SQUID is typically added to act as a low temperature amplifier [Wel93]. This method significantly reduces the apparent flux noise in the detector SQUID, which is crucial for MMC readout, as the intrinsic noise of a MMC detector should not be lower than that of the readout electronics.

3.2.2 Two-Stage Configuration

Implementing a low temperature amplifier is usually realized through a second stage SQUID, situated between the first stage (detector) SQUID and the room temperature amplifier, as depicted in figure 3.4. Here, the subscripts 's' and 'x' refer to the first and second stage, respectively. The first stage SQUID, also referred to as a Front-End SQUID, is typically operated in a voltage bias for this two-stage setup. This can be achieved by connecting a gain resistor R_g in parallel with both the Front-End and the input coil of the amplifier SQUID. If a bias current $I_{b,s}$ is injected into the circuit, all the current will flow through the Front-End, as long as it stays superconducting. Once it becomes normal conducting by further increasing $I_{b,s}$, the current will start shifting to R_g , whose resistance is chosen to be much smaller than the dynamic resistance R_{dyn} of the first stage SQUID, until most of the current flows through R_g . At this point, the resulting voltage across both components becomes approximately constant. This behavior can be visualized through a loadline created by the parallel resistances, which intersects the IVC of the Front-End. The loadline voltage V_s between both extremal IV curves will then remain nearly constant, as the slope is given by the small gain resistance R_g . If a detector signal is now coupled into the Front-End through the input coil with M_{is} , the current in the SQUID will move along the loadline in the $I\Phi$ -plane, corresponding to the externally induced flux Φ_s . The attached input coil of the second stage SQUID would experience these current changes, hence creating a flux change $\Delta\Phi_x$ in the amplifier SQUID, which is operated in a current bias. To maximize the amplification, the second stage SQUID is typically realized as a N -SQUID series array consisting of N serially connected identical SQUID cells. This results in a large voltage drop across the array, given by $V_{array} = NV_{cell}$. Analogous to the single stage readout, the signal will then be amplified at room temperature and fed back to a feedback coil with mutual inductance M_{fs} to compensate for the initial flux change $\Delta\Phi_s$. An additional feedback coil with mutual inductance M_{fx} , spanning symmetrically across every SQUID cell couples a constant flux offset through a bias current I_{Φ_x} into the array in order to maintain it at its working point. The resulting two-stage $V_x\Phi_s$ -characteristic will strongly depend on the flux gain defined as

$$G_\Phi = \frac{\partial\Phi_x}{\partial\Phi_s} = \frac{M_{ix}}{R_g + R_{dyn}} V_{\Phi_s} \approx \frac{M_{ix}}{R_{dyn}} V_{\Phi_s}, \quad (3.8)$$

which relates the flux change induced in the second stage SQUID with a given flux change in the detector SQUID. For $\Delta\Phi_x = \Delta I_s M_{ix} > \Phi_0/2$, additional minima and maxima emerge. These start to overlap for $\Delta\Phi_x > \Phi_0$, thereby creating multiple working points that prevent a practical FLL operation. This sets an upper limit for the flux gain, however, it should be chosen as large as possible to reduce the appar-

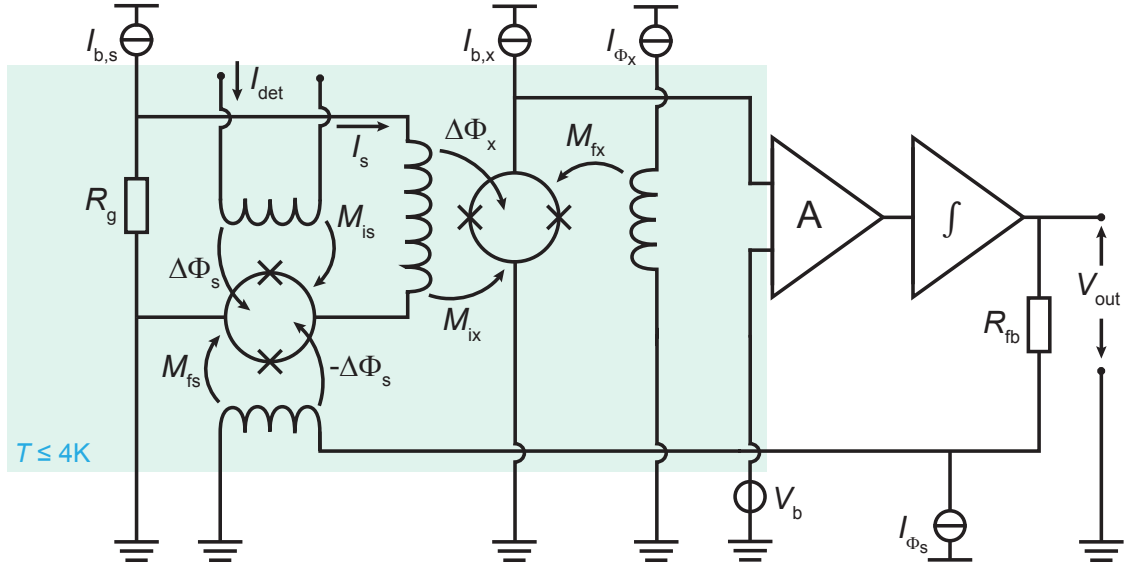


Figure 3.4: Schematic circuit diagram of a two-stage dc-SQUID based readout. The first stage consisting of the detector SQUID is connected in parallel with a gain resistor R_g . The detector signal I_{det} induces a current change ΔI_s and therefore a flux change $\Delta\Phi_x$ in the second stage SQUID, which acts as a low temperature preamplifier. In FLL mode, the signal will be fed back to compensate for the initial flux change $\Delta\Phi_s$, thereby linearizing the detector signal. Choosing an N-SQUID series array amplifies the voltage swing and transfer coefficient, thus significantly reducing the overall apparent flux noise in the detector SQUID.

ent flux noise of the Front-End SQUID. An optimal flux gain has been calculated to $G_\Phi \approx \pi$, corresponding to $\Delta\Phi_x \approx \Phi_0/2$ [Dru96a].

The two-stage setup contributes additional noise sources to equation 3.7, namely the gain resistor and the amplifier SQUID. However, the resulting conversion to the flux Φ_s of the detector SQUID significantly reduces the influence of the room temperature amplifier, which in turn strongly improves the overall signal to noise ratio. The total apparent flux noise of the Front-End then reads [Dru96a]

$$S_{\Phi_s, \text{SQ}} = S_{\Phi_s} + \frac{4k_B T R_g}{G_\Phi^2 (R_g + R_{\text{dyn}})^2} M_{\text{ix}}^2 + \frac{S_{\Phi_x}}{G_\Phi^2} + \frac{S_{V,\text{el}}}{G_\Phi^2 V_{\Phi_x}^2} + \frac{S_{I,\text{el}}}{G_\Phi^2 I_{\Phi_x}^2} + \frac{S_{I,\Phi_x} M_{\text{fx}}^2}{G_\Phi^2} . \quad (3.9)$$

The second term describes the Nyquist current noise caused by the gain resistor, which becomes negligible with a voltage biased detector SQUID where $R_g \ll R_{\text{dyn}}$. The low temperature amplifier (array), the feedback coil current source as well as the room temperature amplifier contributions are reduced by the flux gain param-

eter, which can't be chosen arbitrarily large as mentioned above. However, using a SQUID array for the second stage increases the voltage swing and thus the transfer coefficient by an N -fold, i.e. $V_{\Phi_x} = NV_{\Phi_{\text{cell}}}$, where the subscript 'cell' refers to a single array SQUID cell. Consequently, the total noise level can be further reduced by choosing a high number N of SQUID cells. Here it is noteworthy, however, that these considerations only account for the magnetic flux in a single cell, as otherwise the transfer coefficient would remain constant [Sta93],[Fog93]. Now, using equation 2.39 we obtain for the SQUID array flux noise

$$\sqrt{S_{\Phi_x}} = \frac{\sqrt{S_{V_x}}}{V_{\Phi_x}} = \frac{\sqrt{NS_{V_{\text{cell}}}}}{NV_{\Phi_{\text{cell}}}} = \frac{1}{\sqrt{N}}\sqrt{S_{\Phi_{\text{cell}}}} , \quad (3.10)$$

hence the intrinsic noise of the second stage gets reduced by a factor of $\frac{1}{\sqrt{N}}$ [Sta93]. This also has a consequence for the coupled energy sensitivity of the SQUID array, which is calculated by summing the array flux noise over all N cells, giving

$$\epsilon_{c,x} = N \frac{S_{\Phi_x}}{2L_{\text{cell}}k_{i,\text{cell}}} = \frac{S_{\Phi_{\text{cell}}}}{2L_{\text{cell}}k_{i,\text{cell}}} . \quad (3.11)$$

Where the parameter $k_{i,\text{cell}}$ denotes the coupling of a cell with inductance L_{cell} to its respective input coil segment. Connecting N SQUIDs in series did therefore not affect the energy sensitivity, provided that $k_{i,\text{cell}}$ remains constant across the array. The arrays produced in this working group either contain 16 [Kem15] or 18 [Kra23] cells. Applying this to equation 3.9, we would reduce the above-mentioned contribution of the room temperature amplifier flux noise of $4.13 \mu\Phi_0/\sqrt{\text{Hz}}$ to $0.29 \mu\Phi_0/\sqrt{\text{Hz}}$ and $0.26 \mu\Phi_0/\sqrt{\text{Hz}}$ for $N = 16$ and $N = 18$, respectively. Provided an optimal flux gain of $G \approx \pi$, the noise contribution would further decrease to $0.09 \mu\Phi_0/\sqrt{\text{Hz}}$ or $0.08 \mu\Phi_0/\sqrt{\text{Hz}}$, well below the typical noise level of a detector SQUID.

Besides the improvement of the noise behavior, a major advantage of a two-stage readout setup consists of the low power dissipation produced by the detector SQUID. As opposed to the current bias operation in a single-stage setup, the Front-End is held at a constant, low voltage, such that the dissipated power given by $P = UI$ only consists of approximately 1 nW [Dru07]. However, this amount poses a problematic heat source for low temperature detectors consisting of up to millions of temperature-sensitive calorimeter pixels, such that using a two-stage setup for each pixel is unfavorable. For these, a different approach using time- or frequency-division dc-SQUID multiplexing is followed. These readout techniques constitute a research focus in this working group in order to optimize the readout of several experiments such as the ECHo experiment [Gas17].

3.3 Metallic Magnetic Calorimeters

Low temperature detectors used in this working group exhibit detector arrays consisting of metallic magnetic calorimeters pixels, which are able to absorb and detect photons (X-rays) or heavy particles. The focus of this thesis is to improve the dc-SQUID based MMC readout, which is why we first briefly cover the working principle of such calorimeters.

A general overview of the detector setup can be seen in figure 3.5. The upper part consists of a particle absorber, which, following the law of energy conservation, converts the energy E of an incoming particle into a change in temperature ΔT in the absorber. A paramagnetic sensor is directly attached below, submerged in a weak magnetic field. Strong thermal coupling allows for an effective temperature increase in the sensor, which is given by the total heat capacity C_{tot} of both the sensor and the absorber, resulting in

$$\Delta T \approx \frac{E}{C_{\text{tot}}} . \quad (3.12)$$

Not shown in figure 3.5 is an underlying thermal bath weakly linked to the sensor, which reverts the temperature change by an exponential decay of the signal until the thermal equilibrium is reached. The paramagnetic nature of the sensor changes its magnetization $M(T)$ upon a temperature rise, according to the Curie law $M \propto \frac{1}{T}$ for low temperatures. This induces a magnetic flux change $\Delta\Phi$ proportional to ΔM , which is detected by a meander-shaped pickup coil that is strongly coupled to the sensor. The input coil of the SQUID is directly connected to the pickup coil forming a flux transformer, thereby enabling the readout of the created current signal ΔI_{det} . With equation 3.12 we can write for the induced flux in the SQUID

$$\Delta\Phi_s \propto \Delta\Phi \propto \Delta M \approx \frac{\partial M}{\partial T} \frac{E}{C_{\text{tot}}} , \quad (3.13)$$

provided the deposited energy E is small. Evidently, it is desirable to both reduce the heat capacity and increase the magnetization gradient in order to maximize the flux change $\Delta\Phi$. Another important aspect are short signal rise times that can be realized by a high thermal conductivity of the sensor and the absorber, which is particularly crucial for coincidence measurements. All these material-dependent requirements are fulfilled for the normal conducting metal gold as an absorber material and gold or silver for the sensor. The latter needs to be doped with a few hundred ppm of the rare-earth metal erbium in order to obtain paramagnetic properties. State-of-the-art MMCs of this kind are successfully developed in this working group, providing an exceptional energy resolution, a large energy bandwidth and fast signal rise times

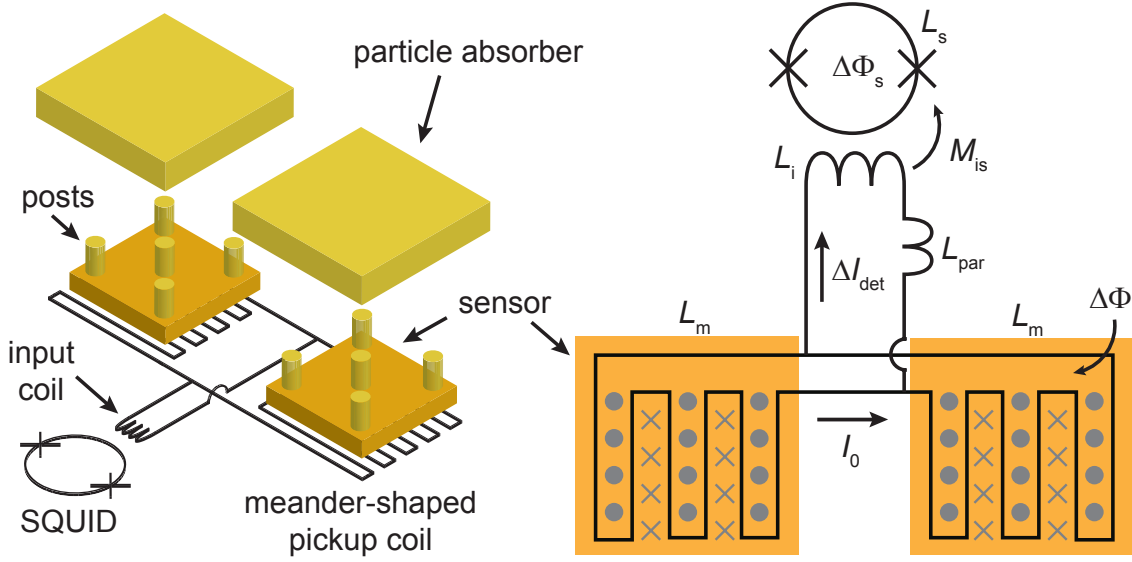


Figure 3.5: Schematic depiction (left) and circuit diagram (right) of a common MMC channel consisting of two pixels. The planar particle absorber is fabricated on top of the paramagnetic sensor, separated by cylinder-shaped posts to prevent energy losses through athermal phonons, while still providing good thermal coupling. Below the sensors two meander-shaped pickup coils connected in parallel detect the flux change $\Delta\Phi$, which can be precisely measured with a SQUID as a flux transformer. The grey dots and crosses within the meander mark a magnetic field induced by the bias current I_0 . The figure was adapted from [Bau22].

well below 100 ns [Kem18].

The detector geometry shown in figure 3.5 is widely used in this working group. Two meander-shaped pickup coils, each with an inductance L_m , are connected as a parallel gradiometer and are located beneath their respective sensor pixel, with a connection to the input coil of the flux transformer. As the SQUID is typically placed far away to mitigate the influence of its heat dissipation, a parasitic inductance L_{par} needs to be taken into account due to the wiring between the SQUID and the detector (figure 3.5, right). A constant small bias current I_0 is injected into the pickup coils to provide the weak bias field needed for the paramagnet. If now a particle gets detected by one of the absorbers, a flux change $\Delta\Phi$ and thus a current is induced in the meander. By applying Kirchhoffs first law and knowing that magnetic flux in a closed superconducting loop is conserved [Lan60], we can calculate the resulting current signal in the input coil to [Bur04]

$$\Delta I_{\text{det}} = \frac{\Delta\Phi}{L_m + 2(L_i + L_{\text{par}})} . \quad (3.14)$$

A significant advantage of this setup lies in the fact, that only one SQUID is needed to readout two pixels. The gradiometer geometry ensures, that depending on which absorber gets hit, the current ΔI_{det} will flow in one direction or the other. Thus, every pixel can be assigned a polarity of the resulting flux in the SQUID loop, making them distinguishable. Together with the mutual inductance $M_{\text{is}} = \frac{\Delta\Phi}{\Delta I_{\text{det}}}$ between the input coil and the SQUID loop, we can now introduce the flux-to-flux coupling

$$\frac{\Delta\Phi_s}{\Delta\Phi} = \frac{M_{\text{is}}}{L_m + 2(L_i + L_{\text{par}})} , \quad (3.15)$$

which by considering equation 3.1 is maximal for $L_i = \frac{L_m}{2} + L_{\text{par}}$. This crucial parameter is a measure for the flux gain and gives therefore information about the quality of the readout setup. Consequently, it is desirable to choose the optimal input coil inductance L_i for a given pickup coil inductance $L_p = \frac{L_m}{2}$.

3.3.1 Extrinsic Energy Sensitivity

In this regard it is reasonable to discuss the noise behavior for this readout setup. Since noise can couple in both directions, the intrinsic flux noise of the SQUID will also couple into the pickup coil, creating the apparent flux noise $\sqrt{S_{\Phi_{s,p}}}$ in the detector. To quantify this noise influence, we define the extrinsic energy sensitivity with respect to a given pickup coil inductance L_p analogous to equation 2.38 as [Knu88]

$$\epsilon_p = \frac{S_{\Phi_{s,p}}}{2L_p} . \quad (3.16)$$

Here, it is necessary to point out that the choice of a single coil with inductance L_p adds a factor of 2 to equations 3.14 and 3.15, such that the flux-to-flux coupling reads

$$\frac{\Delta\Phi_s}{\Delta\Phi_p} = \frac{M_{\text{is}}}{L_p + L_i + L_{\text{par}}} . \quad (3.17)$$

This advantage in coupling, however, does not outweigh the above-mentioned benefit to readout two pixels with one read-out electronic, as the gradiometric design also cancels out unwanted signals through changes in external magnetic field or substrate temperature [Man21]. In the following we consider the case for a single pickup coil

with inductance $L_p = \frac{L_m}{2}$. The presence of a flux transformer is accompanied with a shielding effect with respect to the SQUID loop, such that the geometric inductance is reduced to an effective inductance given by [Gro16]

$$L'_s = L_s(1 - k_{is}^2 s_i) , \quad (3.18)$$

where $s_{in} = \frac{L_i}{L_i + L_p + L_{par}}$ denotes the screening factor [Cla04], which reaches the value of 0.5 for the condition $L_i = L_p + L_{par}$ that maximizes the flux-to-flux coupling. By now using the relation $\frac{\Delta\Phi_s}{\Delta\Phi_p} = \frac{\sqrt{S_{\Phi_s}}}{\sqrt{S_{\Phi_{s,p}}}}$, we finally obtain with equation 3.16 to 3.18 the extrinsic energy sensitivity [Knu88]

$$\epsilon_p = \frac{S_{\Phi_s}(L_i + L_{par} + L_p)^2}{2L_p M_{is}^2} = \frac{S_{\Phi_s}(L_i + L_{par} + L_m/2)}{L_s k_{is}^2 s_i L_m/2} . \quad (3.19)$$

This parameter is minimized by maximizing the flux-to-flux coupling $\frac{\Delta\Phi_s}{\Delta\Phi_p}$ as well as minimizing the intrinsic flux noise of the SQUID S_{Φ_s} given by the expressions derived in subsection 2.2.4. Finding the minimum for the latter provides optimal values for the shunt resistors R_s and the SQUID loop inductance L_s , as we will see in the following section.

4. dc-SQUID Design

The main objective for this thesis was the optimization of an existing Front-End SQUID design for an improved coupling to one of the detectors developed in this working group. As we have seen in the previous section 3.3, adjusting L_i to the detector coil ensures the maximization of the flux-to-flux coupling and therefore minimizes the extrinsic energy sensitivity. The parasitic inductance L_{par} , that arises from the aluminum bonds between the SQUID and the detector substrate to form the flux transformer, has been estimated to 0.5 nH [Hen17]. The previous SQUID design exhibits a design value of $L_i = 1.64$ for the input coil inductance [Bau22], which therefore fulfills the condition $L_i = L_p + L_{\text{par}}$ for the pickup coil inductance of the ECHO-100k detector of $L_p = 1.14 \text{ nH}$ [Man21]. Other MMC detectors from this working group such as the 4k-pixel molecule camera MOCCA and the X-ray detector maXs100 require higher input inductances, as their pickup coil inductances are $L_p = 8.8 \text{ nH}$ and $L_p = 6.65 \text{ nH}$, respectively. In [Bau22] SQUIDs with matching input inductances for the MOCCA and maXs100 detector were developed for the first time using an intermediary coupling transformer. These improved the energy resolution ΔE_{FWHM} of the detectors, although the effect was minimal for the latter. Specifically for the maXs100 detector, a different approach was therefore followed in the framework of this thesis to achieve a better coupling while avoiding a significant increase of the detector noise.

4.1 dc-SQUID with a Two-Turn Input Coil

Increasing the input coil inductance can be realized either by changing the geometry of the coil itself, or by implementing a double flux transformer structure, with the benefit of easily adapting the inductance independently of the SQUID design. The latter, however, was accompanied with a reduction of the effective coupling constant k'_{is} in the work of [Bau22] regarding the maXs100 detector readout, which led to a lower flux-to-flux coupling despite the higher inductance of $L'_i = 5.47 \text{ nH}$. Only the white noise reduction of the SQUID, which was caused by the shielding effects of the added flux transformer, resulted in a small overall improvement of ϵ_p and ΔE_{FWHM} . In this work we designed a new detector SQUID with *window-type* Josephson junctions, which is based on the design developed in [Bau22]. These type of junctions are realized by structuring window-shaped vias on top of the square junction area, which connects the junction with the overlying niobium layer. A schematic of this new SQUID is shown in figure 4.1. Four large oval loops form the second order

gradiometer described in subsection 3.1.1, where the lower fabricated niobium layer (Nb1) contains the SQUID loop as a parallel gradiometer. The feed line coming from the top supplies the serially connected input coil, which was fabricated as a second niobium layer (Nb2) on top of the SQUID loop, only separated by an insulating SiO_2 layer. This geometry allows to combine a small SQUID loop inductance $L_s = \frac{L_1}{4}$ with a large input inductance $L_i = 4L_1$. Also in the Nb2 layer, another serial gradiometer of second order representing the feedback coil is located below the input coil as shown in figure 4.1, with feed lines on the bottom left. This coil has a design inductance of $L_f = 336 \text{ pH}$ with a line width of $3 \mu\text{m}$. Both coils exhibit the same geometry as the corresponding underlying washer strip to maximize the overlap and therefore the coupling. At the same time, the proximity to the input coil is kept at a minimum to minimize cross talk between the two coils. The feed lines of the SQUID loop at the bottom center lead to the junction area, which is shown in the zoomed in section. Both square-shaped Nb/Al-AlO_x/Nb junctions are realized with the dimensions $4.5 \mu\text{m} \times 4.5 \mu\text{m}$ and a targeted critical current of $I_c = 6 \mu\text{A}$, leading to a critical current density of $j_c = 30 \text{ A/cm}^2$. Two AuPd junction shunt resistors R_s are located on the left and right side of the junction area, respectively. Both are attached to a large heat sink made of two gold layers, a thick galvanized layer on top of a sputtered, thin one. These so-called *cooling fins* provide a better electron-phonon coupling thanks to their large volume, which reduces the electron temperature of the normal-conducting shunts and thus mitigates the corresponding thermal noise [Maz24]. A third AuPd resistor R_d with the same dimensions as the shunt resistors is placed above the junction area and connected in parallel with the washer loop. This so-called *washer shunt* provides damping properties to reduce quality factors of parasitic resonances, as will be discussed in section 4.2.

As opposed to the previous design, this input coil is realized with two turns instead of one. Neglecting the stripline inductance L_{str} (see section 5.3), the input inductance becomes approximately proportional to the number of turns squared n^2 [Ket81, Jay81], giving a theoretical value of $L_i^{\text{theo}} \approx 2^2 \cdot 1.64 \text{ nH} \approx 6.56 \text{ nH}$. To implement the second turn a wider washer loop line width of $w_s = 10 \mu\text{m}$ was needed. The line width of the input coil w_i with two turns remained at $3 \mu\text{m}$, which would have not been possible to fabricate on top of the previous washer width of $w_s = 5 \mu\text{m}$ without sacrificing coupling strength. A general increase in w_i , however, entails the risk of capturing noise inducing flux vortices. These form if the B-field pointing perpendicular to the SQUID plane exceeds a critical field given by [Kui08]

$$B_{v,\text{crit}} = 1.65 \frac{\Phi_0}{w_s^2} . \quad (4.1)$$

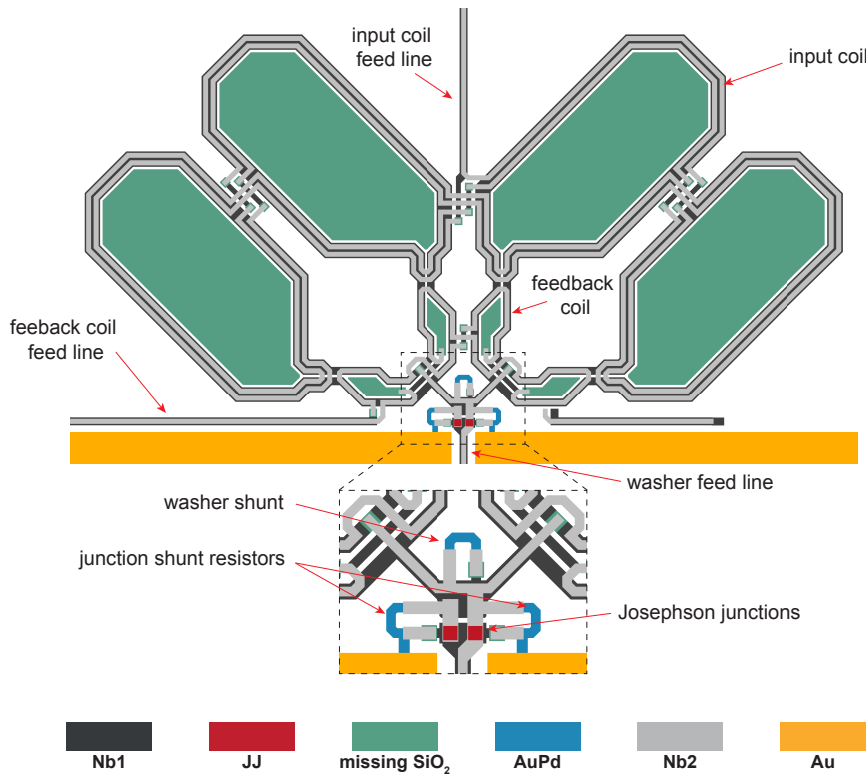


Figure 4.1: (Hier kommt noch ein Mikroskop Bild dazu wie bei Fabian) Schematic of the new dc-SQUID design with a two-turn input coil, including a zoom into the junction area (bottom). Four large oval-shaped loops follow the microstrip transmission line structure given by the washer SQUID loop in the lower niobium layer Nb1 and the input coil in the upper niobium layer Nb2. Fabricated in the same manner is a small feedback coil between the junction area and the input coil. Both coils are free of SiO₂, visualized through the inverse drawing of the SiO₂ layer.

At the earth's surface, its magnetic field reaches a maximum amplitude of $65 \mu\text{T}$, which would give a threshold width of $w_s = 7.2 \mu\text{m}$. The dilution refrigerators used to cool down both the SQUIDs and the detectors typically provide magnetic shielding, such that we consider a width of $w_s = 10 \mu\text{m}$ to have a negligible impact on the flux noise attributed to flux vortices. As the input inductance was the only parameter necessary to adjust, we attempted to keep the other design parameters unaltered. The widened washer width would therefore need to be compensated with an approximately 15 % larger washer hole circumference in order to maintain the same SQUID loop inductance. For the sake of safety, the circumference was increased only by 10 % to prevent possible hysteretic behavior, that can occur if the SQUID loop inductance L_s and therefore the screening parameter β_L grows too large. The

increase was estimated by modeling the rather complicated oval washer loop geometry as a ring-shaped structure whose inductance can be calculated with the relation $L = \mu_0 R \left(\ln \left(\frac{8R}{a} \right) - 2 \right)$, where R denotes the loop radius and a the radius of the wire [Den16]. In addition to these geometric adjustments, a comprehensive structuring of the SiO₂ layer in the area of the washer loops was also omitted, allowing the empty interior to remain free from the insulating layer. This intends to prevent potential flux noise induced by unavoidable magnetic impurities in the SiO₂. The same method was applied to the smaller loop areas formed by the feedback coil. The absence of insulation within the loops is visualized by the green-colored areas in figure 4.1.

The design values for R_s and L_s are chosen such that the extrinsic energy sensitivity given in equation 3.19 is minimized, which requires the maximization of the flux-to-flux coupling ($L_i = L_p + L_{\text{par}}$) and the minimization of the intrinsic white noise of the SQUID. In [Bau22] this numerical calculation was done with the constraints $\beta_C \leq 0.7$ and $\beta_L \leq 1$ to avoid hysteretic behavior, which led to the optimal parameters $\beta_C = 0.7$ and $\beta_L = 0.86$. Consequently, additional noise through voltage jumps caused by hysteretic IVCs as well as Nyquist noise from higher harmonics of the Josephson frequencies [Cla96] have been neglected for this minimization, which was not the case for the derivation of equation 2.40. The intrinsic white noise of the SQUID used for the numerical calculation is therefore given by the adjusted expression [Knu88]

$$S_{\Phi_s} = 2k_B T \frac{L_s^2}{R_s} \left[(1 - k_{is}^2 s_{in})^2 + \frac{\sqrt{2}(1 + \beta_L)^2}{\beta_L^2} \right] . \quad (4.2)$$

To achieve the targeted critical current of $I_c = 6 \mu\text{A}$ with the given junction dimension of $4.5 \mu\text{m} \times 4.5 \mu\text{m}$, we chose a critical current density of $j_c = 29.63 \text{ A/cm}^2$. The current density can be used to calculate the junction capacitance C by using the empirical relation $\frac{1}{C'} = p_1 + p_2 \log_{10} j_c$, where p_1 and p_2 are constant fit parameters [Mae95]. Here, the intrinsic capacitance C' excludes any parasitic capacitances arising from the window-type fabrication technique. For simplicity reasons, we assume $C \approx C'$ and thus obtain $C = 0.95 \text{ pF}$. The optimal Stewart McCumber and screening parameter then provide the values $R_s = 6.3 \Omega$ and $L_s = 147 \text{ pH}$, respectively. The designed shunt resistor in both the previous and the new design was rounded to 6Ω , which results with Ohm's circuit law in a normal resistance of $R_n = 3 \Omega$ for the whole SQUID. This consequently corresponds to a slightly lower damping parameter of $\beta_C = 0.62$. The coupling constant was set to an upper limit of $k_{is} = 0.75$, which is typically the highest achievable value for the SQUIDs produced in this working group. Under the assumption of k_{is} being maximal and $L_i = L_p + L_{\text{par}} = 7.15 \text{ nH}$ for the maXs100 detector read-out, the theoretically obtainable flux-to-flux coupling regarding a single pickup coil is $\frac{\Delta\Phi_s}{\Delta\Phi_p} = 5.38\%$. Lastly, for the extrinsic energy sen-

sitivity we would obtain with equation 4.2 $\epsilon_p = 0.53 h$, given the typical detector operation temperature of $T = 20 \text{ mK}$.

4.2 Damping Methods

As discussed in subsection 2.2.5, several SQUID parameters can be optimized to mitigate the influence of various resonances in the circuit. However, we would like to choose these parameters accordingly to the minimization of the extrinsic energy sensitivity as discussed in the previous section 4.1. This choice imposes substantial limitations on the extent to which additional parameter modifications can be implemented. For instance, increasing the length of the input coil l_i would shift the corresponding strip line resonance given by equation 2.45 away from the operation frequency, which in turn would lead to a larger input inductance, thus impeding the maximization of the flux-to-flux coupling. Furthermore, even resonances far away from the operation frequency can result problematic as thermally activated transitions between different states increase the noise level [Sep87]. This motivates to follow a more practical approach to suppress LC resonances, which can be realized through damping with attenuators, such as the damping resistor R_d shown in the top of junction area in figure 4.1. These are typically connected in parallel to the resonant circuit, as this reduces the quality factor Q of the corresponding LC resonance given an appropriate dimensioning of the resistor. Consequently, the $L_s C_p$ and $L_s C$ resonances can be damped by implementing a *washer shunt* R_d [Ono97, Ryh92]. Although the IVC intersection caused by the latter could not be fully eliminated in previous works of this group, they showed a significant smoothing of the curves as the accompanying step structures decreased [Bau18]. The current noise introduced through this resistor, on the other hand, deteriorates the energy sensitivity and thus limits the damping benefit. However, this effect is minimal for the condition $R_d \approx R_s$ with $\beta_L = 1$ [Enp86, Ryh92], which is why we choose $R_d = 6 \Omega$. The input circuit is shunted with an $R_x C_x$ attenuator to damp the $L_i C_p$ resonance, where the added capacitance C_x blocks low frequency current noise [Sep87]. Both damping techniques to suppress C_p -related resonances were proven to be effective for various SQUID designs in many works [Knu87, Enp86, Can91, Bau18]. As for the $\lambda/2$ resonances, both the R_d and the $R_x C_x$ attenuator provide good damping as well [Can91], since they terminate the microstrip lines and thus avoid impedance mismatches given a suitable dimensioning of the resistors (see section 5.3). A schematic of the resulting circuit diagram of the coupled dc-SQUID with all damping components is depicted in figure 4.2 (left). Shown on the right is the design of the $R_x C_x$ shunt, which has been adapted from [Bau22]. The capacitance $C_x = 10 \text{ pF}$ is divided into two parallelly connected square-shaped capacitors with $\frac{C_x}{2}$ to reduce the space needed on the chip.

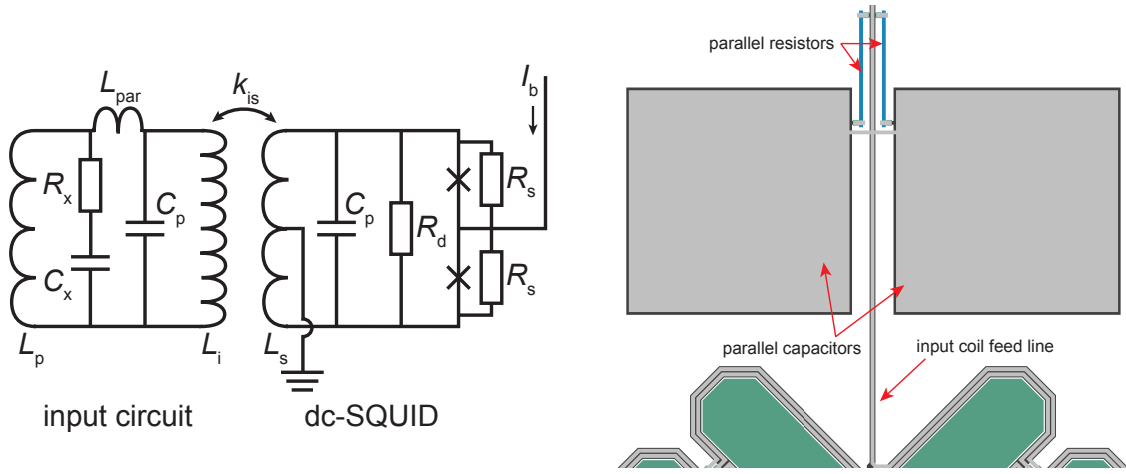


Figure 4.2: Left: Schematic circuit of a coupled dc-SQUID with damping components R_d and R_xC_x . The input coil forms a flux transformer with a pickup coil of inductance L_p . The parasitic capacitance between the input circuit and the SQUID loop is connected in parallel to both L_i and L_s . Right: Structure design of the R_xC_x attenuator located above the dc-SQUID. Both devices R_x and C_x are each realized as two parallel components. (Beschriftungen werden noch hinzugefügt)

The top and bottom plate of each capacitor are fabricated in the Nb2 and Nb1 layer, respectively. The shunt R_x is split as well into two parallel AuPd resistors with $2R_x$ each. Optimal values for these components will be discussed in chapter 5.

4.2.1 Lossy Input Coil

Although the above-mentioned damping methods provide significant improvement regarding the resonance behavior, further suppressing individual resonances is, depending on the SQUID design, typically favourable or even necessary. For this reason, we apply two additional damping techniques, which require resistive gold layers electrically or inductively coupled to the circuit. The former will be covered in the following, whereas the latter is explained in subsection 4.2.2.

Several approaches to reduce Q values of $\lambda/2$ resonances associated with microstrip lines have been investigated in [Boy22]. The experimental setup consists of two parallel meanders with each having a length of 6.5 mm and an inductance of 2 nH. They are fabricated on top of each other with insulating SiO_2 between them and in a direct-coupled MMC setup, where as opposed to the flux transformer setup in section 3.3, the SQUID is directly coupled to the sensor. This setup produced high Q resonances at integer and half-integer wavelengths. Whereas placing an individual resistor in parallel to one meander only damped the half-integer modes, a more

distributed damping scheme in the form of an insulated gold layer between both meanders provided strong damping of all microstrip resonances while maintaining a low detector noise level. The Q values have been further reduced by structuring the Au layer with the same geometry as the microstrip lines and electrically connecting it to one of the meanders, thereby preventing large noise inducing, normal-conducting loops. The attenuation constant α of this lossy microstrip line increases with frequency and thickness of the Au layer, while the noise stays insensitive upon thickness changes.

Within the scope of this thesis, such damping techniques were implemented and tested on the dc-SQUID described in section 4.1. For this, we sputtered a gold layer between SiO_2 and Nb2 with the same geometry as the input coil running above the SQUID loop. This gold layer was omitted around the vias between the washer loops to avoid additional normal resistances. Gold and niobium were structured together as a bilayer in the same microfabrication step by sputtering the upper niobium layer directly after the gold. To connect the four input coil segments over vias, the original second niobium layer Nb2 was used. A schematic of our Front-End design with this lossy input coil, including an image obtained with an optical microscope, is shown in figure 4.3. Our Front-End SQUIDs with this gold layer adjacent to the input coil will be referred to as 'lossy' for the upcoming discussions.

4.2.2 Inductive Damping

Together with the attempt of suppressing resonances through a lossy microstrip line, we introduce a second new damping technique denoted as inductive damping. This method is based on the principle of magnetic damping, where a change in magnetic flux creates eddy currents in a nearby conductor, which following Lenz's law induces a flux trying to compensate the initial one. The flux change is therefore damped by effectively transferring part of the magnetic energy to the kinetic energy of the induced current, which in the case of a normal conductor emits heat. This phenomenon also causes the reduction of the geometric inductance of the SQUID loop due to the shielding effect of the flux transformer (see subsection 3.3.1). A strong indicator that this mechanism can be applied to SQUIDs shows the first mentioned experiment in [Boy22], where a square gold layer representing the MMC sensor was placed at a height of 300 nm above an isolated meander. This lead to a significant reduction of the high Q values of the meander modes. The concept is now applied to the feed lines on our SQUID chip, where large gold pads have been placed across the SQUID washer and feedback coil feed lines, as shown in figure 4.4. The sharp voltage spikes associated with high Q resonances, that can be present within those lines would therefore be damped by partly converting their energy into heat in the normal conducting gold layer. The gold pads are fabricated in the same layers as the

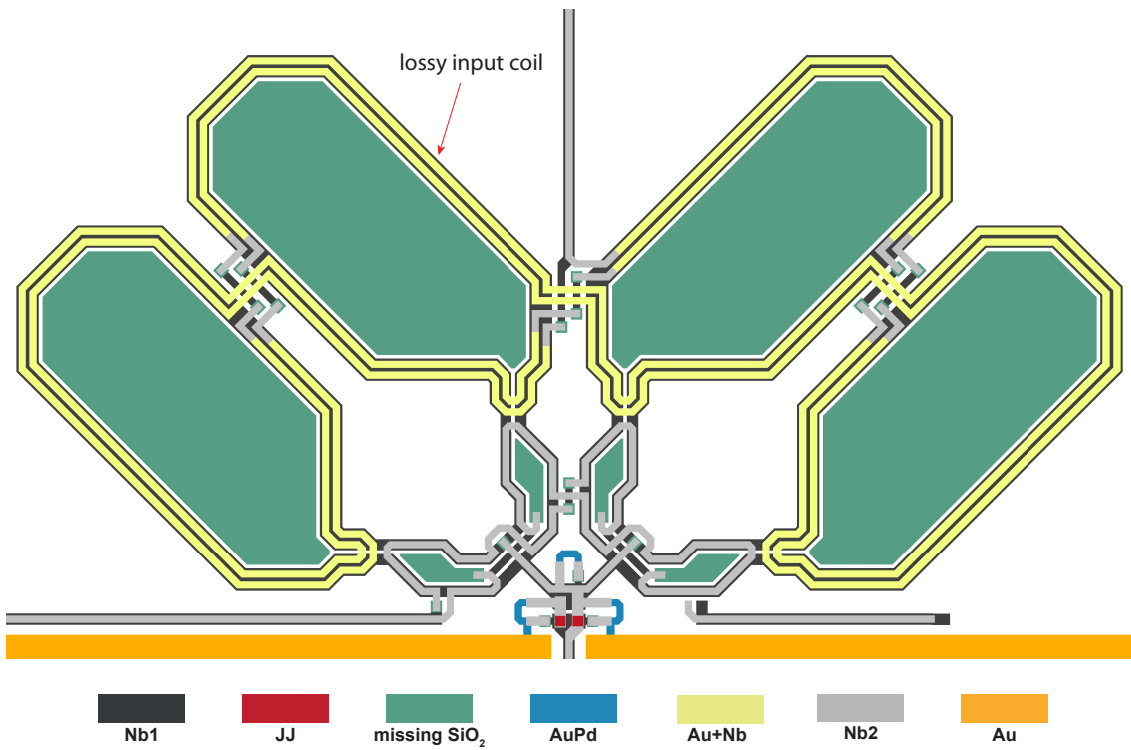


Figure 4.3: (siehe figure 3.1) dc-SQUID design with a two-turn input coil realized as a lossy microstrip line. A gold layer is structured between the insulating SiO_2 and an upper niobium layer and has been fabricated in a single step as a bilayer. The overlying niobium in the Nb2 layer connects all four input coil segments over their respective washer loop to prevent the vias to acquire a normal resistance.

heat sinks for the shunt resistors and are consequently sputtered first before being electroplated. The latter step significantly increases their volume, which allows for larger and more effective eddy currents. Additionally, the generated heat is expected to better dissipate into the chip substrate as the electron-phonon coupling increases with volume. All feed lines are typically realized as microstrip lines, but for this case we adjusted them into a coplanar structure as there is no insulation layer after Nb2. Figure 4.4 shows the chip design consisting of four distinct Front-End variants, each provided with the inductive damping scheme. The first channel at the top is realized without an input coil in order to better allocate possible resonance structures visible in the SQUID's IVCs. The design introduced in 4.1, also referred to as 'non-lossy', is represented in channel 2, followed by the lossy variant in channel 3. The last channel contains a lossy Front-End as well, however, the washer loop interiors were not kept SiO_2 -free. This allows to investigate the influence of possible magnetic impurities in the insulation material and assess whether it can be regarded as negligible or not. The same chip design has been produced with and without gold pads on the

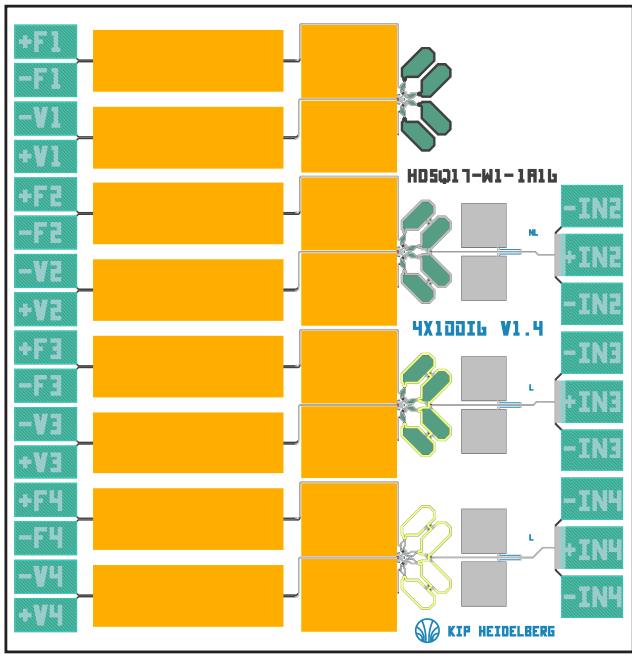


Figure 4.4: (siehe figure 3.1 ...) Inductive damping scheme on the Front-End SQUID chip of the type 4x100i6 v1.4. All feedback coil and SQUID loop feed lines are covered with large rectangular, insulated gold pads. Each SQUID channel is occupied with a different SQUID variant. Channel 1: Front-End without an input coil. Channel 2: Non-lossy SQUID design presented in section 4.1. Channel 3: Lossy SQUID design from section 4.2.1. Channel 4: Lossy design with SiO_2 inside the washer loop interiors.

feed lines, resulting in 8 different Front-End SQUIDs that were developed and tested within the scope of this thesis. We present our results in the following chapter.

5. Experimental Results

This chapter provides an overview over the general performance of the dc-SQUIDs developed within the framework of this thesis. Particularly, the resonance behavior and the noise spectra were investigated. We begin with a summary of characteristic parameters obtained by our measurements and compare them with the target values. The noise measurement has been conducted with the two-stage setup at $T = 10\text{ mK}$ in the cryostat, whereas the single-stage measurements to obtain characteristic front-end properties have been done both in the helium vessel and the cryostat.

5.1 Characteristic dc-SQUID Parameters

Despite all distinctions between the front-end variants mentioned in chapter 4, most characteristic parameters such as the SQUID loop inductance L_s or shunt resistance R_s are unaffected by these variations. We, therefore, consider the following measurements to be representative for all variants and assume possible variations to be caused from fabrication-related variations across the wafer.

Figure 5.1 shows the current-voltage as well as the voltage-flux characteristics of one of the measured SQUIDs. This SQUID (chip no. HDSQ17-W1-3C16) is of the type 'non-lossy' with inductive damping and has been measured at a cryostat temperature of $T = 10\text{ mK}$. First, we measured the slope of the IV curves across the ohmic regime, which allows to determine the normal resistance R_n of the SQUID. In total 10 SQUIDs from the wafer HDSQ17-W1 covering all variants we measured. The median normal resistance taken from these SQUIDs yields the value $R_n = 3.0\Omega$, with the largest deviation being 13.3 %. This corresponds to a shunt resistance of $R_s = 2R_n = 6.0\Omega$, which exactly corresponds to the targeted value.

The maximum voltage swing as seen in figure 5.1 (right) is obtained by applying a bias current I_b^{\max} supplied by the SQUID electronics, while driving a ramp signal through one of the coupled coils to provide a varying external flux. This yielded median values of $\Delta V_{\max} = 29.95\mu\text{V}$ and $I_b^{\max} = 11.62\mu\text{A}$. For $T = 0\text{ K}$, I_b^{\max} should correspond to twice the critical current I_c (compare figure 2.9). Due to the finite temperature we obtain noticeable thermal smoothening visible in the IVC of figure 5.1 (left), such that the critical current is better approximated by [Dru96b]

$$I_c \approx \frac{I_b^{\max}}{2} + \frac{k_B T}{\Phi_0} \left(1 + \sqrt{1 + \frac{I_b^{\max} \Phi_0}{k_B T}} \right) . \quad (5.1)$$

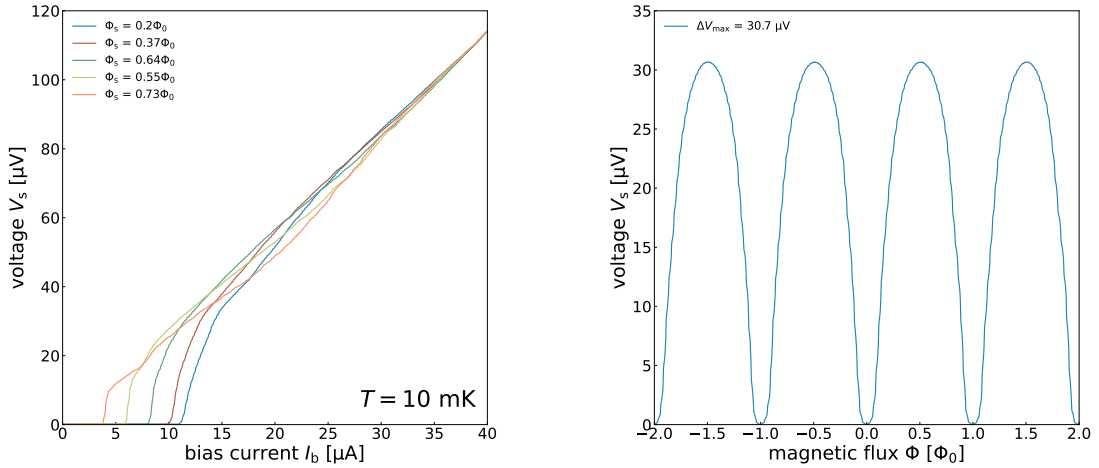


Figure 5.1: Current-voltage (left) and voltage-flux characteristics (right) of a non-lossy SQUID with inductive damping (chip no. HDSQ17-W1-3C16). The extremal IV curve with the lower critical current $I_{c,1}$ does not correspond exactly to $\Phi = (n + \Phi_0/2)$, which is a consequence of an asymmetric current injection. The $V\Phi$ curve was measured at $I_b^{\max} = 11.33 \mu\text{A}$, resulting in a maximal voltage swing $\Delta V_{\max} = 30.7 \mu\text{V}$. Note that both plots have different scaling on the V -axis.

We, therefore, calculate the median critical current to $I_c = 5.84 \mu\text{A}$. With a junction size of $4.5 \mu\text{m} \times 4.5 \mu\text{m}$, this corresponds to a critical current density of $j_c = 28.8 \text{ A/cm}^2$, such that both values only deviate 2.7 % from the design values $I_c = 6 \mu\text{A}$ and $j_c = 30 \text{ A/cm}^2$. The junction capacitance thus becomes slightly smaller than the design value according to the empirical relation introduced in section 4.1. Using the empirical dependence $1/C' = 0.132 - 0.053 \log_{10} j_c$ for the intrinsic junction capacitance C' obtained in [Bau22] and by again assuming $C' = C$, we get the capacitance $C = 0.948 \text{ pF}$, which is in excellent agreement with the target value of 0.95 pF . The McCumber parameter can now be calculated to $\beta_C = 0.61$, also fitting well with the design value of 0.62.

As for the transfer coefficients, different values for the positive and negative slopes of the $I\Phi$ curve are expected due to the asymmetric current injection, which is realized by differing SQUID loop inductances between each arm of the loop, ultimately leading to a unilaterally larger transfer coefficient I_Φ [Fer15]. The measured values are $I_{\Phi,+} = 10.2 \mu\text{A}/\Phi_0$ and $I_{\Phi,-} = 23.1 \mu\text{A}/\Phi_0$ for the positive and negative slope, respectively. The voltage transfer coefficient is approximately symmetric (compare figure 5.1) and yields $V_{\Phi,+} = 94.0 \mu\text{V}/\Phi_0$ and $V_{\Phi,-} = 93.0 \mu\text{V}/\Phi_0$. The variance of these transfer parameters is rather large, with deviations from the median of up to

39 %. These results are nevertheless comparable to previous SQUIDs produced in this working group [Ric17].

Screening parameter β_L

The screening parameter is typically derived by using the β_L -dependent normalized current swing $\Delta I_{\max}/2I_c$ at $V = 0$, which has been numerically simulated in [Tes77]. We estimated the current swing by extrapolating both extremal IV curves for the theoretical case of $T = 0$, thus neglecting the thermal rounding and obtaining a minimal and maximal critical current $I_{c,1}$ and $I_{c,2}$. The median of the maximal current swing ΔI_{\max} yields $7.18 \mu\text{A}$, ranging from $6.09 \mu\text{A}$ to $7.73 \mu\text{A}$ for the lowest and highest measured value. The value for ΔI_{\max} , which approximately corresponds to the current swing of the voltage-biased SQUID in a two-stage configuration, indicates that the SQUID is well adapted to the arrays produced in this working group. These arrays have a typical reciprocal mutual inductance of $1/M_{ix} = 11.7 \mu\text{A}/\Phi_0$, such that the flux $\Delta\Phi_x$ coupled to the array is $\Delta\Phi_x = M_{ix}\Delta I_{\max} = 0.61 \Phi_0$, which is close to the optimal value of $\Phi_0/2$ to achieve a flux gain of $G_\Phi \approx 3$ (see section 3.2.2). The current swing of each SQUID allows us to calculate the median screening parameter to $\beta_L = 0.65$, which is rather low compared to the design value of $\beta_L = 0.86$, indicating an overestimation of the SQUID loop inductance L_s . According to the obtained β_L and β_C , hysteretic behavior should not occur and thus be absent in the IVCs. The intersections and current steps seen in figure 5.1, therefore, likely stem from resonances, which will be discussed in section 5.3.

SQUID loop inductance L_s

With the above-determined I_c and β_L values we obtain a median SQUID loop inductance of $L_s = 108 \text{ pH}$. This represents a significant deviation of 27 % from the target value of $L_s = 147 \text{ pH}$ discussed in section 4.1, which can be partly explained by the conservative estimation for the geometric adjustment of the washer loop size, resulting in a smaller inductance. On the wafer HDSQ17-W1 we included for comparison the original design [Bau22] with a single turn input coil, where we measured two channels of the chip HDSQ17-W1-3A09. These provided the respective values $L_s = 128 \text{ pH}$ ($\beta_L = 0.80$) and $L_s = 138 \text{ pH}$ ($\beta_L = 0.87$), which is in accordance with the value of 135 pH that was measured in [Bau22]. This confirms that the washer loops were designed too small, resulting in a smaller SQUID loop inductance than the targeted 147 pH . The measured value of 108 pH , however, fits well with the simulated value of 106 pH , which was simulated with InductEx after the SQUIDs were already produced. The reduction of L_s reduces the coupling M_{is} between input

coil and SQUID loop, which in turn reduces the flux-to-flux coupling $\Delta\Phi_s/\Delta\Phi$ and thus the extrinsic energy sensitivity ϵ_p given by equations 3.17 and 3.19, respectively.

Mutual inductances

The mutual inductances of the input and feedback coil were obtained by sending a current ramp to the corresponding coils. The input coil was only connected to the SQUID electronics during the measurements in the helium vessel at 4.2 K, where M_{is} was measured from 22 front-end channels from 9 chips, covering all non-lossy and lossy variants. The measured median values are $M_{is} = 611 \text{ pF}$ and $M_{fs} = 51 \text{ pF}$, where the latter coincides well with the measured value of 50 pF from [Bau22], as it is expected because the geometry of the feedback coil was not changed. The input coil current sensitivity is almost twice as large as the value determined with the previous design with a single-turn input coil, which yielded $M_{is} = 328 \text{ pF}$ [Bau22]. This result is expected from the general linear dependence of the mutual inductance on the number of turns n of the input coil and the SQUID loop inductance, i.e. $M_{is} \approx nL_s$ [Ket81].

The fact that $M_{is}(n = 2)/M_{is}(n = 1) < 2$ can be explained by two reasons. On the one hand, the inductance L_s has been reduced by approximately 19 % as compared to the previous design, which according to equation 3.1 leads to a decreased current sensitivity M_{is} . On the other hand, the geometric two-turn input coil structure might deteriorate the coupling constant k_{is} , as compared to a single turn design.

Taking into account the input inductance calculated in section 5.2 and the other parameters determined above, we can calculate the coupling constant via equation 3.1 to $k_{is} = 0.73$, which is close to the target value 0.75 that has been set as a realistic upper limit for the minimization of the extrinsic energy sensitivity ϵ_p . This suggests that the reduction of the input coil current sensitivity M_{is} is mostly due to the smaller SQUID loop inductance L_s . It is noteworthy, however, that the variations of both the measured critical currents and the current swings were rather large with up to 11 % and 15 %, respectively. This of course provides an uncertainty for β_L and L_s that needs to be taken into account. Such variances have also been observed in [Bau22], where it was shown that SQUIDs with *cross-type* junctions exhibit a smaller variance across the wafer, making them more reliable than window-type junctions regarding I_c .

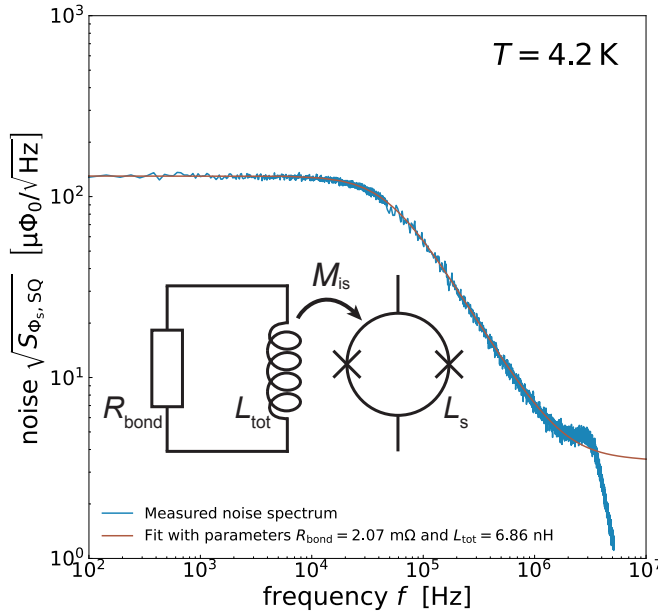


Figure 5.2: Noise spectrum of the input coil inductance L_i measurement. The input coil is resistively shorted through aluminum bond wires with resistance R_{bond} , which results in thermal noise that couples into the SQUID. The added noise has a cut-off frequency $f_c = R_{\text{bond}}/(2\pi L_{\text{tot}})$ that allows to extract the added white noise component by a numerical fit. The input inductance can be derived by subtracting the parasitic inductances from L_{tot} , which is a fit parameter alongside R_{bond} .

5.2 Input Coil Inductance

To determine whether the new SQUID design with increased input inductance exhibits better coupling to the maXs100 detector, it is essential to measure the input coil inductance L_i . For this measurement, the input coil is electrically shorted via its bond pads with aluminum bond wires while the front-end is in a two-stage setup at 4.2 K. In this special case, the detector SQUID was part of an integrated chip that contains both the new non-lossy front-end design as well as an array for the second stage, which has been developed and tested in [Kra23]. These integrated chips were produced on the wafer HDSQ16-W1 and were designed with the same material thicknesses, such that we expect the measurement to be representative for the non-lossy SQUIDs from HDSQ17-W1. The aluminum bond wires are normal conducting at the temperature of 4.2 K and thus provide a resistance R_{bond} . The closed loop couples frequency-independent thermal noise from the resistive wires into the SQUID loop via the mutual inductance M_{is} , which adds to the apparent noise of the first stage SQUID. The resistance R_{bond} forms an RL lowpass filter together with the total inductance L_{tot} consisting of the input coil, its feed line and the wire inductance. The attributed cut-off frequency damps higher noise frequencies up to the point where this noise contribution becomes negligible, as can be seen in the measured noise spectrum of figure 5.2. The second cut-off at a frequency around 5 MHz represents the lowpass characteristic of the SQUID electronics, as it provides a limited bandwidth of up to 6 MHz. The total apparent noise of the Front-End SQUID is then given by

$$S_{\Phi_s, \text{SQ}} = M_{is}^2 \frac{4k_B T}{R_{\text{bond}}} \left[\frac{1}{1 + (\frac{2\pi f L_{\text{tot}}}{R_{\text{bond}}})^2} \right] + S_{\Phi_s, w} , \quad (5.2)$$

where the first term describes the additional current noise of the shorted circuit, which is schematically shown in the inset of figure 5.2. The second term represents the apparent white noise of the SQUID. This expression is numerically fitted to the measured data to obtain both the resistance of the bonding wires and the total inductance L_{tot} . Two measurements from separate chips (2C14 and 2C23) were carried out, where the one from 2C14 is depicted in figure 5.2. The fits result in $R_{\text{bond}}^{2\text{C}14} = 2.07 \text{ m}\Omega$ and $L_{\text{tot}}^{2\text{C}14} = 6.86 \text{ nH}$ for the chip 2C14, whereas $R_{\text{bond}}^{2\text{C}23} = 1.86 \text{ m}\Omega$ and $L_{\text{tot}}^{2\text{C}23} = 6.74 \text{ nH}$ for the chip 2C23. For the aluminum wires it has been shown in [Hen17] that they, depending on their arrangement, exhibit an inductance of $L_{\text{bond}} \approx 0.14 \text{ nH/m}\Omega$, which consequently results in $L_{\text{bond}}^{2\text{C}14} = 0.29 \text{ nH}$ and $L_{\text{bond}}^{2\text{C}23} = 0.26 \text{ nH}$. The parasitic inductance from the input coil feed lines can be estimated with the microstrip inductance per unit length [Cha79]

$$L_{\text{str}} = \mu_0 \frac{h + 2\lambda}{w_i + 2h + 4\lambda} , \quad (5.3)$$

with λ being the London penetration depth of the superconductor, w_i the width of the upper line and h the thickness of the insulating layer. The length of the feed lines is approximately $724 \mu\text{m}$, the width $3 \mu\text{m}$ and SiO_2 has been fabricated as a 375 nm thick layer. We also assume $\lambda = 90 \text{ nm}$, which is a typical value for the fabricated niobium in this working group. This yields a small contribution of 0.12 nH for the feed line inductance. Thus, we finally obtain the input inductances $L_i^{2\text{C}14} = 6.45 \text{ nH}$ and $L_i^{2\text{C}23} = 6.36 \text{ nH}$. These are only slightly smaller than the originally targeted value of $L_i^{\text{theo}} \approx n^2 1.64 \text{ nH} \approx 6.56 \text{ nH}$ mentioned in section 4.1. However, two effects overestimate the expected value. On the one hand, the measured inductance of the previous design only yielded 1.27 nH . On the other hand, the approximation does not take the additional microstrip inductance L_{str} into account (see section 3.1), which grows only linearly with n rather than n^2 [Ket91]. This effect would reduce the increase of L_i upon adding a second turn. In contrast to that, a third effect leads to an underestimation of the target value. The enlargement of the washer loop has a strong influence on L_i due to the series connection of the input coil, where the resulting inductance increase per washer loop is multiplied by 4. Taking all effects into account, the enlargement of the washer loops should lead to additional 0.48 nH per turn, which after multiplying by n^2 results in the average input coil inductance $L_i = 6.40 \text{ nH}$ obtained from the two measurements. With InductEx we obtained a simulated value of $L_i = 5.6 \text{ nH}$, which deviates 13 % and 12 % from $L_i^{2\text{C}14}$ and $L_i^{2\text{C}23}$, respectively. These moderate deviations are in accordance with previous inductance

simulations in several works of this working group [Fer15, Bau22]. For the following discussions, we will use the average $L_i = 6.40 \text{ nH}$ of the two measurements.

An overview of the most relevant measured parameters compared to their respective design values is given by table 5.1, showing an overall good agreement.

Parameter	R_s [Ω]	I_c [μA]	M_{is} [pH]	M_{fs} [pH]	L_s [pH]	L_i [nH]	β_L	β_C	k_{is}
Measured	6	5.84	611	51	108	6.40	0.65	0.61	0.73
Design	6	6	-	50	147	6.56	0.86	0.62	0.75

Table 5.1: Summary of measured characteristic parameters of the new dc-SQUID design with a two-turn input coil, which are compared with the corresponding target values.

5.3 Resonance Behavior

In this section we will investigate how various LC resonances might affect the IVCs of the SQUIDs tested in the previous section and whether the applied damping techniques proved to be effective or not. Figure 5.3 showcases the IVCs of 8 distinct SQUIDs from the 10 chosen for the characterization. The order from top to bottom corresponds to the order shown in the inductively damped chip with various SQUID types in figure 4.4. These damped SQUIDs are on the right side (e) through h), while the corresponding SQUID types without inductive damping are on the left side (a) through d)) in the same order. There are a few differences between certain SQUID variants, however, they collectively share a prominent feature at $V_s \approx 40 \mu\text{V}$. This artifact shows a pronounced current step with corresponding intersections between the IV curves. The fact that it is also present in the SQUIDs without input coil (d) and h)) rules out any input coil related resonances to be the underlying cause. Regarding the feedback coil, due to the small serially connected inductance its resonance $f_{L_f}C_p$ lies far above the operation frequency, as we will see in the following. Consequently, we attribute the pronounced current step at approximately $40 \mu\text{V}$ to the fundamental SQUID resonance $f_{L_s}C$, which by using equation 2.44 is calculated to $f_{L_s}C = 22.2 \text{ GHz} = 46 \mu\text{V}/\Phi_0$, using the measured values of $L_s = 108 \text{ pH}$ and $C = 0.95 \text{ pF}$. This value does not exactly correspond to the observed $40 \mu\text{V}$, which would indicate an underestimation of either the SQUID loop inductance L_s , junction capacitance C or both. As discussed in section 5.1, the parasitic capacitance arising from the insulation window structure of the junction is typically neglected, i.e. $C = C'$. The real junction capacitance should therefore be slightly larger, leading to a decreased resonance frequency $f_{L_s}C$. The measured inductance L_s can also deviate

from the real value, which could be explained by the asymmetric $I\Phi$ characteristic as this aspect has not been included in the numerical simulation for $\Delta I(\beta_L)$ in [Tes77]. Additionally, the error of L_s is dominated by the measurement uncertainty regarding the maximal current swing. Further measurements are needed to increase the accuracy of the approximated value.

The comparison of each side of figure 5.3 demonstrates a significant smoothening of all IVCs of the inductively damped SQUIDs, as compared to their non-damped counterparts. We can therefore conclude that damping with insulated gold pads proved to effectively suppress all visible resonances to some extent, regardless of the SQUID design. Consequently, one would expect the resulting intrinsic flux noise of the damped SQUIDs to be lower. This will be investigated in section 5.4. Whether the various step structures apart from the large step at $40\mu\text{V}$ can be assigned to the different microstrip and LC resonances described in subsection 2.2.5 will be the subject of the following discussion.

For the C_p -related resonances, we need to take into account that the SQUID loops are connected in parallel and the input coil in series. The parasitic capacitance C_p^{loop} per washer loop will therefore need to be multiplied by a factor of 4 or 1/4 to obtain the total parasitic capacitance C_p . A theoretical value has been calculated to [Enp91, Enp92]

$$C_p^{\text{loop}} = \frac{l_{i,1/4} C_{\text{str}}}{8} = \frac{l_{i,1/4}}{8} \frac{\epsilon_0 \epsilon_r w_i K_f(w_i, t_i, h)}{h} , \quad (5.4)$$

where $l_{i,1/4}$ denotes the input coil length on a single washer loop and C_{str} the microstrip line capacitance per unit length. The latter depends on the vacuum and relative permittivity ϵ_0 and ϵ_r , as well as the width of the input coil w_i , the fringing factor $K_f(w_i, t_i, h)$ and the insulation thickness h . The fringing factor also depends on w_i , h and the thickness of the input coil denoted as t_i [Cha79]. With $h = 375\text{ nm}$, $w_i = 3\text{ }\mu\text{m}$ and a sputtered Nb2 layer with $t_i = 400\text{ nm}$ we obtain the value $K_f = 1.45$. In case of the lossy SQUID variants, the niobium thickness of the input coil only yielded $t_i = 200\text{ nm}$, leading to $K_f = 1.42$. This has a small effect on the resulting resonance frequencies calculated below, as they only deviate approximately 2 % from the respective frequencies obtained for the non-lossy type. For the sake of clarity, we will therefore only consider the non-lossy SQUID in the following discussion, which will qualitatively represent the lossy type as well.

With a fringing factor of $K_f = 1.45$, we obtain a microstrip inductance of $C_{\text{str}} = 0.4\text{ nF}$. The input coil length per washer loop is approximately given by $l_{i,1/4} \approx l_i/4 \approx 860\text{ }\mu\text{m}$, with the total length of the input coil being $l_i \approx 3.44\text{ mm}$. Consequently,

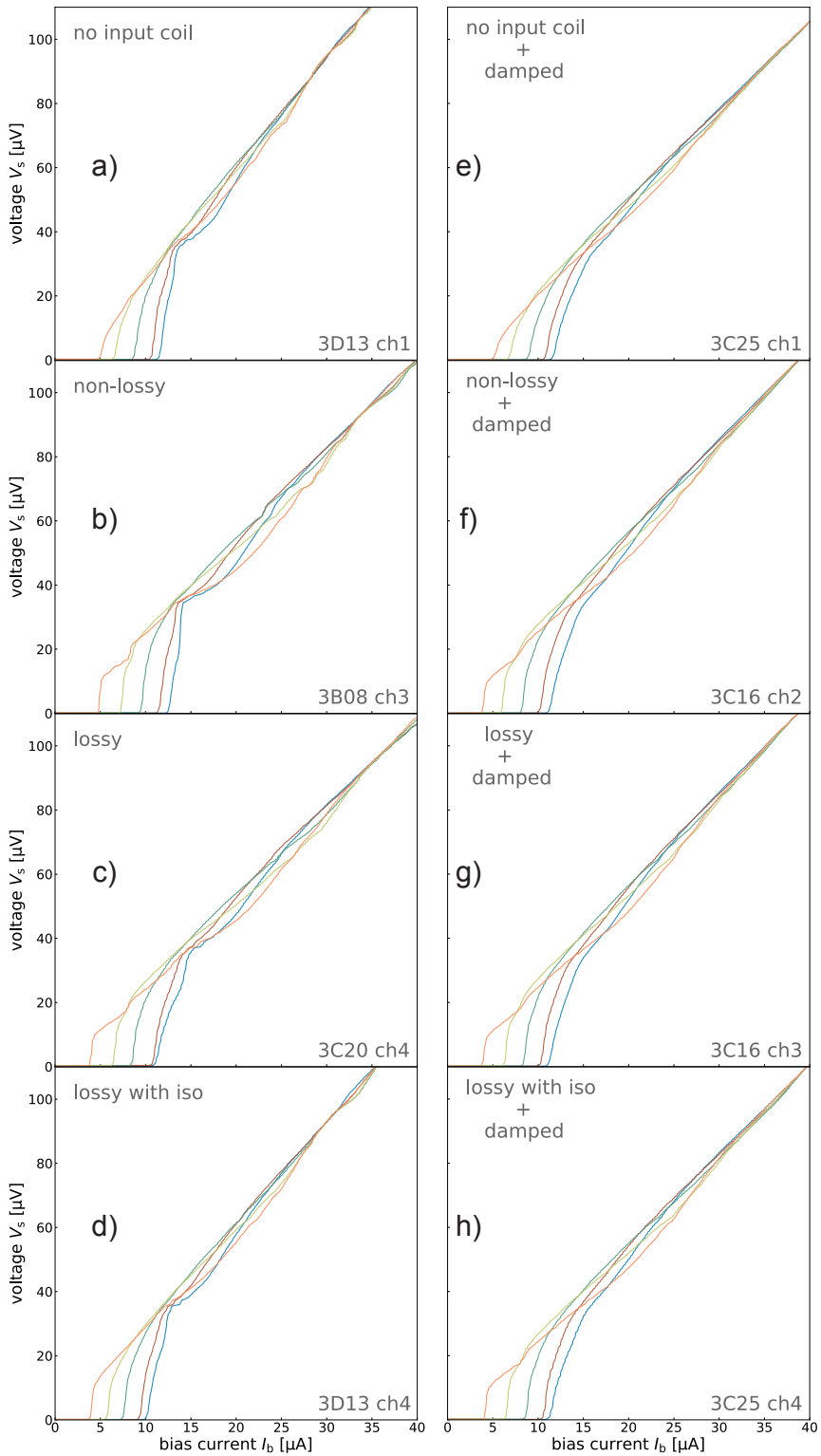


Figure 5.3: a) - d): Measured IVCs of the SQUID types presented in figure 4.4 in the same order, but without inductive damping. e) - h): The same measurement for the respective SQUID types but with inductive damping. Measured at $T = 10$ mK.

we obtain for the parasitic capacitance per washer loop $C_p^{\text{loop}} = 0.043 \text{ pF}$. The total parasitic capacitance regarding the washer is therefore $C_p = 4C_p^{\text{loop}} = 0.17 \text{ pF}$, which is still small compared to the junction capacitance $C = 0.95 \text{ pF}$, i.e. $C_p/C \ll 2$. The influence of this parameter on the energy sensitivity should consequently be small, as explained in subsection 2.2.5. The $L_s C_p$ resonance can now be calculated to $f_{L_s C_p} = 1/(2\pi\sqrt{L_s 4C_p^{\text{loop}}}) = 34 \text{ GHz}$, where we used the measured SQUID loop inductance $L_s = 108 \text{ pH}$. This corresponds to a voltage drop of $V_s = 70.2 \text{ }\mu\text{V}$ for the condition $f_J = f_{L_s C_p}$. This is well above the optimal operation frequency given by $f_{\text{op}} \approx 0.3f_c \approx 5.1 \text{ GHz}$ ($V_s = 10.5 \text{ }\mu\text{V}$), with $f_c = I_c R_s / \Phi_0$ [Can96]. Mostly the plots a) through c) from figure 5.3 showcase small distinctive step-like structures around $75 \text{ }\mu\text{V}$. These could, however, also stem from a higher harmonic of the fundamental SQUID resonance, which should be the case for the SQUID without input coil (a)), as there is no corresponding parasitic capacitance.

For the $f_{L_i C_p}$ resonance we need to take the $R_x C_x$ attenuator into account. The capacitances C_x and C_p can approximately be added up to the total capacitance $C_{\text{tot}} = C_x + \frac{C_p^{\text{loop}}}{4}$ due to the serial connection of the input coil. The geometric input coil inductance is shielded analogously to L_s (compare equation 3.18), giving the relation $L'_i = (1 - k_{is}^2 s_s) L_i$ [Can96]. Here, the screening factor was derived to $s_s = \frac{\beta_L s_i k_{is}^2}{6+2\beta_L+\beta_L s_i k_{is}^2}$. The input inductance and pickup coil inductance also form a parallel connection, resulting in $L_{\text{tot}} = \frac{L'_i L_p}{L'_i + L_p}$. The resonance frequency then reads

$$f_{L_i C_p} \approx \frac{1}{2\pi\sqrt{C_{\text{tot}} L_{\text{tot}}}} , \quad (5.5)$$

which by using our measured and calculated parameters yields 0.9 GHz . The corresponding voltage drop is $V_s = 1.8 \text{ }\mu\text{V}$, which is well below the above-mentioned operation voltage and is therefore not visible in the IVCs from figure 5.3. The capacitance C_x is chosen small to minimize the attributed $Q_{L_i C_p}$ value, which for an RCL parallel circuit is given by

$$Q_{L_i C_p} \approx R_x \sqrt{\frac{C_{\text{tot}}}{L_{\text{tot}}}} \approx \frac{R_x}{f_{L_i C_p} L_{\text{tot}}} . \quad (5.6)$$

Evidently, C_x cannot be chosen arbitrarily small as it would shift the resonance to the vicinity of the working point. An optimal value has been found to be $Q_{L_i C_p} \approx 2$ [Can96]. The resistive component of the attenuator is typically dimensioned such that it corresponds to the nominal impedance Z_0 of the microstrip line in order to mitigate wave reflections occurring where the input coil leaves the SQUID loop. This impedance can be expressed as [Enp91]

$$Z_0 = \sqrt{\frac{L_{\text{str}}}{C_{\text{str}}}} . \quad (5.7)$$

With the produced geometric proportions of the microstrip, the optimal value yields $R_x = 20.6 \Omega$, which was chosen as the design value. Therefore, with equation 5.6 we obtain an optimal capacitance of $C_x = 31 \text{ pF}$. Unfortunately, such a large capacitance has not yet been implemented into the new design. We adapted the lower value of the previous design (10 pF), which had been chosen in [Bau22] with the premise to work with the pickup coil of the ECHo-100k detector ($L_p = 1.14 \text{ nH}$). In our case we obtain $Q \approx 1.13$, however, the corresponding resonance frequency is still small enough to consider the effect of this resonance as negligible.

We can also further neglect the C_p -related resonance with respect to the feedback coil, as its small design inductance of $L_f = 336 \text{ pH}$ leads to a resonance frequency of $f_{L_f C_p} = \frac{160 \mu\text{V}}{\Phi_0} = 77 \text{ GHz}$, well above f_{op} .

Regarding the $\lambda/2$ resonances a distinction is made whether the input coil or the SQUID loop act as the signal carrying line. They will consequently be referred to as the input coil or washer resonance with the resonance frequencies f_{l_i} or f_{l_w} , respectively. These should ideally fulfill the condition $4f_{l_i} < f_{\text{op}} < \frac{f_{l_w}}{4}$ to mitigate their noise inducing influence at the working point [Can91]. The wave propagation velocity c_{str} depends on L_{str} and C_{str} , such that equation 2.45 becomes [Enp92]

$$f_{l_i} = \frac{c_{\text{str}}}{2l_i} = \frac{1}{2l_i\sqrt{L_{\text{str}}C_{\text{str}}}} . \quad (5.8)$$

With the length of the input coil l_i , we obtain for the input coil resonance $f_{l_i} = \frac{36.4 \mu\text{V}}{\Phi_0} = 17.6 \text{ GHz}$. However, we need to include the length $l_i^{\text{feed}} \approx 620 \mu\text{m}$ of the input coil feed lines which are also structured as a microstrip transmission line. This results in 14.9 GHz and accordingly $V_s = 30.9 \mu\text{V}$. Even though the condition $4f_{l_i} < f_{\text{op}}$ is not fulfilled, there are no visible step structures in the vicinity of this frequency, which suggests successful damping of this microstrip resonance. The effectiveness of the $R_x C_x$ attenuator has also been demonstrated in [Bau22], where drastic step structures at $f_{l_i} = \frac{54 \mu\text{V}}{\Phi_0}$ were eliminated entirely after adding the $R_x C_x$ component to the SQUID design with $L_i = 1.27 \text{ nH}$.

The washer resonance is more difficult to determine for the given SQUID loop design, as the complex washer structure surrounding the junction area affects the effective length l_w of the signal carrying line. A crude approximation can be done by adding the SQUID loop feed line length to the circumference of a single washer loop due to the parallel connection to estimate l_w . We thus obtain $f_{l_w} \approx \frac{50.3 \mu\text{V}}{\Phi_0} = 26.9 \text{ GHz}$, which is more than four times the operation frequency. Just like for f_{l_i} , there aren't

any artifacts in the SQUID IVCs that could be assigned to this resonance. This indicates that the washer shunt exhibits good damping properties, as has already been demonstrated by [Ric17] and [Bau18].

Another prominent step structure seen in the IVCs of figure 5.3 occurs at approximately $15\text{ }\mu\text{V}$ for the extremal curve with the smallest critical current $I_{c,1}$. This feature is absent in the IVCs of the SQUIDs without input coil (a) and e)) as well as the previous design with a single-turn input coil (not shown here). Consequently, the second turn seems to cause an additional resonance effect that has not yet been identified. It is also unclear why this artifact does not appear in plot d) of figure 5.3. Interestingly, there are no considerable differences between the characteristics of lossy and non-lossy variants. It is, however, worth noting that the input coils were not shorted or connected to a pickup coil during the experiments described in this chapter, which might be accompanied with an altered resonance behavior. The resonance as well as the noise properties of the new SQUID design with a shorted input coil should therefore be investigated in future works.

5.4 Noise Performance

The noise measurement was conducted at approximately 10 mK in the dilution cryostat, using the two-stage setup described in subsection 3.2.2, where the second stage SQUID is provided by a separate SQUID array chip. Figure 5.4 depicts the two-stage noise measurement of two lossy SQUIDs with SiO_2 inside of the SQUID loop, one without and one with inductive damping from the chips 3A13 and 2A16, respectively. In the following we will use the name of the front-end chip to represent the corresponding two-stage setup. The flux noise $\sqrt{S_\Phi}$ is given as the square root of the power spectral density in and is plotted against the frequency, ranging from approximately 30 mHz to 25 kHz . The measured data is shown as black dots and consists of a frequency-independent white noise and a low frequency $1/f$ noise component, as described by equation 2.43. The fit of the total apparent flux noise are represented by a blue curve. The corresponding fit values are shown in table 5.8, yielding for 3A13 $\sqrt{S_{\Phi,w}} = 0.41\text{ }\mu\Phi_0/\sqrt{\text{Hz}}$ and $\sqrt{S_{\Phi,1/f}(1\text{ Hz})} = 3.9\text{ }\mu\Phi_0/\sqrt{\text{Hz}}$ with an exponent of $\alpha = 0.87$, whereas the fit for 2A16 provided $\sqrt{S_{\Phi,w}} = 0.57\text{ }\mu\Phi_0/\sqrt{\text{Hz}}$, $\sqrt{S_{\Phi,1/f}(1\text{ Hz})} = 4.5\text{ }\mu\Phi_0/\sqrt{\text{Hz}}$ and $\alpha = 0.84$.

These values are, apart from the white noise of 3A13, relatively large which stems from larger contributions from the first and second stage SQUID, as discussed in the following. Both plots additionally contain the individual noise contributions from equation 3.9. To disentangle contributions it is necessary to also perform a noise measurement of the isolated SQUID array within the two-stage setup, which is

Parameter	$\sqrt{S_{\Phi_s,w}}$ [$\mu\Phi_0/\sqrt{\text{Hz}}$]	$\sqrt{S_{\Phi_s,1/f}}(1\text{ Hz})$ [$\mu\Phi_0/\sqrt{\text{Hz}}$]	α	$\epsilon_{s,w}$ [h]	$\epsilon_{s,1/f}$ [h]	$\epsilon_{p,w}$ [h]	$\epsilon_{p,1/f}$ [h]
3A13 (L)	0.23	3.52	0.85	1.58	369.3	25.26	5916
2A16 (LD)	0.30	3.54	0.82	2.68	373.5	43.0	5983
int. chip (NL)	0.42	2.0	0.60	5.26	119.2	84.2	1910
2A02 (L)	0.22	3.0	0.85	1.44	268.2	23.11	4297
transf. (CJJ)	0.38	3.33	0.70	3.45	265.0	114.4	8784

Table 5.2: Overview of the determined noise and energy sensitivities of the SQUIDs described in this section. The acronyms stand for lossy (L), lossy and inductively damped (LD), non-lossy (NL), and cross-type Josephson junctions (CJJ). The latter represents the 6 nH double flux transformer SQUIDs measured in [Bau22].

achieved by driving no currents through either the front-end or its coupled coils. The noise measured by this method corresponds to the apparent flux noise in the array, which is calculated by equation 3.9 for $G_\Phi = 1$, $S_{\Phi_s} = 0$ and $R_{\text{dyn}} = 0$. For the array chip in this operating mode we assumed a temperature of $T = 150\text{ mK}$, which is caused by self-heating. For the shunt resistors determined in section 5.1, we obtain a sheet resistance of $1.23\Omega/\square$. The gain resistance R_g with a length of 0.3 squares thus yields 0.37Ω . The transfer coefficients V_{Φ_x} and I_{Φ_x} are obtained prior to the noise measurement and yield $V_{\Phi_x} = 602.2\mu\text{V}/\Phi_0$ and $I_{\Phi_x} = 11.71\mu\text{A}/\Phi_0$ for 3A13, whereas for 2A16 $V_{\Phi_x} = 762.3\mu\text{V}/\Phi_0$ and $I_{\Phi_x} = 9.02\mu\text{A}/\Phi_0$. The intrinsic flux noise of the array S_{Φ_x} can, therefore, be determined by subtracting the noise terms due to the gain resistor, current source and room temperature amplifier from the measured total noise. For the two-stage setup, the array noise contribution is reduced by the flux gain squared, as explained in subsection 3.2.2. For the measurements displayed in figure 5.4, we obtained $G_\Phi = 2.34$ for the setup with the 3A13 chip and $G_\Phi = 1.31$ for 2A16. This resulted in an array white noise component of $\sqrt{S_{\Phi,w}} = 0.24\mu\Phi_0/\sqrt{\text{Hz}}$ and a $1/f$ component of $\sqrt{S_{\Phi,1/f}}(1\text{ Hz}) = 1.50\mu\Phi_0/\sqrt{\text{Hz}}$ for 3A13, whereas with 2A16 we obtained $\sqrt{S_{\Phi,w}} = 0.31\mu\Phi_0/\sqrt{\text{Hz}}$ and $\sqrt{S_{\Phi,1/f}}(1\text{ Hz}) = 2.44\mu\Phi_0/\sqrt{\text{Hz}}$. The higher noise contribution of the array in the 2A16 setup as well as the lower G_Φ value can be explained by dephasing of the array. This might be prevented in future experiments with better shielding of the experimental setup. Insufficient shielding allows external magnetic flux to be trapped inside the individual SQUID cells during the cooldown of the cryostat. If this added flux bias varies across the cells, the corresponding $V\Phi$ -characteristics of the cells will be out-of-phase, resulting in a deteriorated $V\Phi$ -characteristic of the array, which reduces ΔV_{max} and V_Φ .

For the two-stage measurement we assumed a larger array chip temperature of 500 mK due to the current flowing through R_g , resulting in considerable more dis-

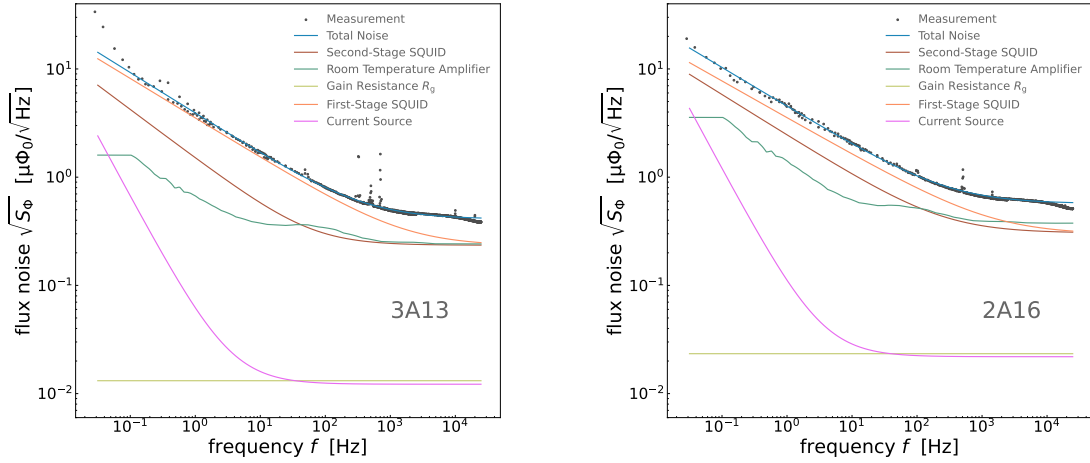


Figure 5.4: Measured noise spectra at $T = 10\text{ mK}$ using a two-stage setup, where the low temperature amplifier is provided by a separate SQUID array chip. The blue curve represents the numerical fit of the measured total noise, whereas the remaining curves are the individual contributions of the first- and second-stage SQUID as well as the SQUID electronics consisting of the room temperature amplifier and the current source. Left: Lossy variant with SiO_2 from the chip 3A13. Right: Lossy variant with SiO_2 , including inductively damped feed lines (2A16).

sipated heat. However, comparing with the array only measurement, the contribution of the gain resistor (yellow curve) is strongly reduced due to $G_\Phi > 1$ and $R_{\text{dyn}} \gg R_g$, thus becoming negligible. The noise contribution of the current source for the array flux bias, shown by the pink curve in figure 5.4, is also negligible. The green curve represents the room temperature amplifier noise, consisting of the current and voltage noise as given by equation 3.9. In the white noise regime it is comparable to the array contribution (brown curve), while for low frequencies the contribution of array noise is larger. The total noise, however, is dominated by the intrinsic noise of the first-stage SQUID (orange curve), which is obtained analogously to the intrinsic array noise by subtracting all residual contributions from the total noise. The resulting fit curves provided the parameters $\sqrt{S_{\Phi,w}} = 0.23\text{ }\mu\Phi_0/\sqrt{\text{Hz}}$ and $\sqrt{S_{\Phi,1/f}}(1\text{ Hz}) = 3.52\text{ }\mu\Phi_0/\sqrt{\text{Hz}}$ with an exponent of $\alpha = 0.85$ for the Front-End of 3A13, whereas the Front-End of 2A16 yielded $\sqrt{S_{\Phi,w}} = 0.30\text{ }\mu\Phi_0/\sqrt{\text{Hz}}$, $\sqrt{S_{\Phi,1/f}}(1\text{ Hz}) = 3.54\text{ }\mu\Phi_0/\sqrt{\text{Hz}}$ and $\alpha = 0.82$. The white noise levels of both Front-Ends are comparable to previous low-noise SQUIDs developed in this working group, however, the low frequency component is slightly larger than the typical value of 2-3 $\mu\Phi_0/\sqrt{\text{Hz}}$. Surprisingly, the intrinsic noise of the first-stage SQUID from 3A13 is

slightly lower than the inductively damped SQUID from 2A16. The smoother IVCs obtained by the inductive damping scheme should have a positive effect on the flux noise level. The extent to which this effect occurs is, however, unclear. The difference of the white noise level between both SQUIDs can also stem from differing SQUID loop inductances L_s , as the noise depends on L_s according to equation 4.2. It is thus crucial to further investigate the noise spectra of all SQUID variants produced within the scope of this thesis to provide a more conclusive comparison.

Two other noise measurements involving the new SQUID design, but with different setups, were conducted in this working group and are now briefly compared to the aforementioned results. The first setup involves an integrated two-stage chip developed and tested in the work of [Kra23], which carries the label HDSQ16-W1-3A15. This chip houses a modified version of the array that was used for our two-stage measurements, where it exhibits 18 SQUID cells instead of 16. Located next to it is the first-stage SQUID, where the non-lossy variant described in section 4.1 has been chosen. The noise measurement was performed with the same two-stage configuration as described above. All noise contributions were determined the same way as well, which resulted in $\sqrt{S_{\Phi,w}} = 0.42 \mu\Phi_0/\sqrt{\text{Hz}}$, $\sqrt{S_{\Phi,1/f}(1 \text{ Hz})} = 2.0 \mu\Phi_0/\sqrt{\text{Hz}}$ and $\alpha = 0.60$ for the intrinsic noise of the Front-End. The larger white noise contribution could be explained by the increased self-heating due to the proximity of the array to the Front-End. Interestingly, in contrast, the low-frequency noise and the corresponding $1/f$ exponent are reduced to the same degree, which are comparable with the SQUIDs produced in this working group. Further noise measurements of the non-lossy variant will allow to assess whether these values are attributed to the integrated two-stage setup or the Front-End design itself.

Lastly, a different type of noise measurement has been conducted by [Maz24], which involved a cross-correlation setup at 10 mK in the cryostat. The setup utilizes two array channels of a single array chip that are connected via their input coils to the Front-End [Her23]. As this method cancels out the array noise, it is possible to directly obtain the intrinsic noise of the detector SQUID. The measured Front-End from the chip 2A02 is of the same type as the one from 3A13 used for our two-stage setup, i.e. lossy with SiO₂. The noise was determined to be $\sqrt{S_{\Phi,w}} = 0.22 \mu\Phi_0/\sqrt{\text{Hz}}$, $\sqrt{S_{\Phi,1/f}(1 \text{ Hz})} = 3.0 \mu\Phi_0/\sqrt{\text{Hz}}$ and $\alpha = 0.85$, which is comparable to the values for the SQUID from 3A13. This measurement was part of a series of temperature-dependent noise measurements, which allowed to determine the minimum temperature T_{\min} of the Front-End chip, as the noise level will not further decrease for a cryostat temperature below that value. The thermal decoupling of the SQUID from the cryostat occurred at $T_{\min} \approx 90 \text{ mK}$, which we will use for the following discussion regarding the energy sensitivity.

5.5 Energy Sensitivity

With the obtained flux noise we are now able to determine the intrinsic and extrinsic energy sensitivities introduced in subsections 2.2.4 and 3.3.1. The theoretical values are obtained by using equation 4.2 for the theoretical intrinsic white noise of the SQUID. For the sake of clarity, they will be compared only to the noise measurement of the 3A13 chip, whereas an overview of the remaining values is given by table 5.3. With the measured parameters discussed in section 5.1 and for the determined chip temperature $T \approx 90 \text{ mK}$ we get $\sqrt{S_{\Phi_{s,w}}^{\text{theo}}} = 0.11 \mu\Phi_0/\sqrt{\text{Hz}}$, which compared to the measured values is reduced by a factor of 2 to 4. This could be explained by added noise that is mixed down due to the resonance-induced hysteretic behavior shown in the IVCs. Additionally, the current noise from the washer shunt is not taken into account in equation 4.2. The measured intrinsic energy sensitivity $\epsilon_{s,w}$ will therefore deviate accordingly, yielding $\epsilon_{s,w} = 1.58 h$, whereas the theoretical value is $\epsilon_{s,w}^{\text{theo}} = 0.36 h$. The measured value of $\epsilon_{s,w}$ is surprisingly low compared to typical values achieved in this working group, however, for the $1/f$ noise the value of $\epsilon_{s,1/f} = 369.3 h$ is rather large. The flux-to-flux coupling $\Delta\Phi_s/\Delta\Phi_p$ regarding a single pickup coil with $L_p = L_m/2 = 6.65 \text{ nH}$ yields 4.51 %, using the obtained values $M_{is} = 611 \text{ pH}$ and $L_i = 6.4 \text{ nH}$. If we consider the gradiometric geometry of the pickup coil of the maXs100 detector, the coupling is reduced by a factor of 2 to $\Delta\Phi_s/\Delta\Phi = 2.25 \%$ (compare subsection 3.3.1). This represents an increase over the value obtained in [Bau22], where the use of a double flux transformer even deteriorated the coupling from 1.95 % to 1.75 %. In [Bau22], the noise with the 6 nH double flux transformer setup with the previous design using both window-type and cross-type junctions, had been measured using the cross-correlation method. The window-type variant exhibited an unexplained increase of the targeted critical current by a factor of 2, which led to strong hysteretic behavior and higher noise. We will therefore restrict the comparison to the cross-type variant, which is labeled 'SQ-CJJ-4w1 Chip10 #1'. The measured noise yields $\sqrt{S_{\Phi_{s,w}}^{\text{theo}}} = 0.38 \mu\Phi_0/\sqrt{\text{Hz}}$ for the white noise, $\sqrt{S_{\Phi_{s,1/f}}}(1 \text{ Hz}) = 3.33 \mu\Phi_0/\sqrt{\text{Hz}}$ for the $1/f$ component and $\alpha = 0.70$. The measured white noise of the new design therefore represents an improvement, which together with the coupling gain will result in an overall smaller extrinsic energy sensitivity. Just like with $\epsilon_{s,w}$, the measured extrinsic energy sensitivity exceeds the predicted value, where we obtain $\epsilon_{p,w}^{\text{theo}} = 5.71 h$ and $\epsilon_{p,w} = 25.26 h$ by using equation 3.19. The $1/f$ contribution results accordingly also in a large value of $\epsilon_{p,1/f} = 5916 h$. These values, however, represent a significant reduction as compared to the previous design with an intermediary coupling transformer. Given the aforementioned parameters, the cross-type version yields $\epsilon_{p,w} = 114.4 h$ and $\epsilon_{p,1/f} = 8784 h$.

To further improve the noise level one could adapt cross-type junctions into the

Parameter	$\sqrt{S_{\Phi_{s,w}}}$ [$\mu\Phi_0/\sqrt{\text{Hz}}$]	$\sqrt{S_{\Phi_{s,1/f}}}(1\text{ Hz})$ [$\mu\Phi_0/\sqrt{\text{Hz}}$]	α	$\epsilon_{s,w}$ [h]	$\epsilon_{s,1/f}$ [h]	$\epsilon_{p,w}$ [h]	$\epsilon_{p,1/f}$ [h]
3A13 (L)	0.23	3.52	0.85	1.58	369.3	25.26	5916
2A16 (LD)	0.30	3.54	0.82	2.68	373.5	43.0	5983
int. chip (NL)	0.42	2.0	0.60	5.26	119.2	84.2	1910
2A02 (L)	0.22	3.0	0.85	1.44	268.2	23.11	4297
transf. (CJJ)	0.38	3.33	0.70	3.45	265.0	114.4	8784

Table 5.3: Overview of the determined noise and energy sensitivities of the SQUIDs described in this section. The acronyms stand for lossy (L), lossy and inductively damped (LD), non-lossy (NL), and cross-type Josephson junctions (CJJ). The latter represents the 6 nH double flux transformer SQUIDs measured in [Bau22].

new SQUID design, which allows the production of up to 4 times smaller junction areas in our own cleanroom. Consequently, the junction capacitance is reduced by a factor of 4, allowing the use of a shunt resistance twice as large without altering β_C . According to equation 4.2, this reduces the noise by a factor of 2. Additionally, the SQUID loop inductance L_s should be adjusted to the target value of 147 pH. This can be implemented by again increasing the size of each washer loop, which would in turn also shift the input coil inductance closer to the optimal value of $L_i = L_p + L_{\text{par}} = 7.15$. This would lead to an increase of the mutual inductance M_{is} and thus the flux-to-flux coupling $\Delta\Phi_s/\Delta\Phi$, thereby further reducing ϵ_p .

6. Summary and Outlook

In this work we introduced a new dc-SQUID design optimized for the readout of the MMC-based X-ray detector maXs100, which is developed in this working group. For this, the design based of the work of [Bau22] was adapted by increasing the input coil inductance to match the inductance of the detector pickup coil. Contrary to the intermediary flux transformer approach tested in [Bau22], the inductance was adjusted by adding a second turn to the input coil. This measure maximizes the flux-to-flux coupling $\Delta\Phi_s/\Delta\Phi$, which is a crucial parameter to maximize the amplitude of the readout signal as well as to minimize the noise coupled into the detector, thereby increasing the energy resolution ΔE_{FWHM} .

To assess whether the design changes lead to additional noise or to a deteriorated resonance behavior, we measured the SQUID both in a single-stage setup to investigate general properties including the current-voltage characteristics, and in a two-stage setup to measure the flux noise. Additionally, we implemented new damping techniques to suppress various resonances originating from either LC resonant circuits or from microstrip structures. These involved the deposition of additional gold onto the washer and feedback coil feed lines, separated by SiO_2 , as well as the fabrication of the input coil as a bilayer containing both gold and niobium. The new SQUID design was produced with different damping scheme configurations to examine the effectiveness of the employed damping approaches.

The single-stage experiments were conducted both in a liquid helium transport vessel at 4 K and in a dilution cryostat at 10 mK. In the case of the latter, we measured the characteristic parameters of 10 SQUIDs, which except for the SQUID loop inductance resulted to be close to their target values. It should be noted, however, that the critical current and consequently β_L and the current swing exhibited a large fabrication-related variance. Furthermore, the measurement uncertainty regarding I_c and ΔI leads to strongly varying values of L_s . We determined a SQUID loop inductance of $L_s = 108 \text{ pH}$, deviating 27% from the target value of 147 pH. This can be explained by the conservative adjustment of the washer loops, which had to be enlarged to compensate for the inductance loss through widening the lines to fit the second input coil turn. Additionally, with the previous SQUID design the inductance L_s had already been overestimated, yielding only 135 pH. This could be confirmed in this work with similar values as the previous design was included on the wafer produced within the scope of this thesis. The input coil inductance, on

the other hand, was measured at 4 K and determined to $L_i = 6.4 \text{ nH}$ as the average of two measurements. This represents a deviation of 14 % from the simulated value of 5.6 nH, which is in agreement with observations from [Fer15, Bau22].

The IVCs of all new SQUID variants presented in chapter 5 were obtained at 10 mK in the cryostat. We compared 8 SQUIDs each with a different damping scheme to explore the influence of the added damping on the resonant structures. The most effective method resulted to be the inductive damping of the feed lines, as it showcased significantly smoother IV curves as compared to the non-damped counterparts. The implementation of the input coil as a lossy microstrip line, however, seemed to provide no considerable reduction of the observed resonance artifacts. It is noteworthy though, that the input coils were in an open loop and not shorted or connected to another coil. This might affect input coil related resonance frequencies, which should be investigated in future works.

The flux noise measurements were performed alongside the IVC measurements in the same cryostat and at the same temperature. Two front-end SQUIDs with lossy input coils, one without inductive damping from the chip 3A13 and one with from the chip 2A16, were measured in a two-stage setup. The obtained intrinsic flux noise of the front-ends were $\sqrt{S_{\Phi,w}} = 0.23 \mu\Phi_0/\sqrt{\text{Hz}}$ and $\sqrt{S_{\Phi,1/f}(1 \text{ Hz})} = 3.52 \mu\Phi_0/\sqrt{\text{Hz}}$ with an exponent of $\alpha = 0.85$ for the front-end without inductive damping and $\sqrt{S_{\Phi,w}} = 0.30 \mu\Phi_0/\sqrt{\text{Hz}}$, $\sqrt{S_{\Phi,1/f}(1 \text{ Hz})} = 3.54 \mu\Phi_0/\sqrt{\text{Hz}}$ and $\alpha = 0.82$ for the inductively damped front-end. Another front-end of the same type as the former has been measured in [Maz24] using a cross correlated setup, which provided comparable values to the front-end from 3A13. The non-lossy variant has been measured in an integrated two-stage setup and yielded, possibly due to selfheating effects, a larger white noise of $\sqrt{S_{\Phi,w}} = 0.42 \mu\Phi_0/\sqrt{\text{Hz}}$, whereas the $1/f$ component resulted in a lower value of $\sqrt{S_{\Phi,1/f}(1 \text{ Hz})} = 2.0 \mu\Phi_0/\sqrt{\text{Hz}}$ with an also smaller exponent of $\alpha = 0.60$. These values are similar to the noise of the previous design in a double flux transformer setup measured in [Bau22]. Further measurements are needed to verify if these values are representative for the respective SQUID type. The results are nevertheless comparable to other low-noise SQUIDs developed in this working group, even though smaller values up to $< 1 \mu\Phi_0/\sqrt{\text{Hz}}$ have been achieved in the low frequency regime [Fer15]. The noise values of the front-end from 2A16 indicate, however, that the inductive damping technique did not significantly raise the overall noise levels, thus posing a promising technique worth pursuing in the future. The flux-to-flux coupling $\Delta\Phi_s/\Delta\Phi$ regarding the maXs100 detector yielded 2.25 %, which represents an increase of 29 % over the value of 1.75 % obtained with the double flux transformer in [Bau22]. Consequently, our extrinsic energy sensitivities are compar-

atively low, where the best value regarding the white noise yielded $\epsilon_{p,w} = 23.11 \text{ } h$ and regarding the $1/f$ noise $\epsilon_{p,1/f} = 1910 \text{ } h$.

A possible measure to further increase the flux-to-flux coupling while also reducing the white noise would be a better adjustment of the SQUID loop and input coil inductance, which can be realized by expanding the washer loop size. Furthermore, substituting window-type with cross-type junctions allows for the use of shunt resistances twice as large, leading to a significant reduction of the intrinsic white noise by a factor of 2. The four times smaller junction capacitance would also shift the fundamental SQUID resonance further away from the working point, ensuring optimal performance. Nevertheless, the new SQUID design represents an improved detector SQUID for the maXs100 detector and should be preferably used in the future.

Bibliography

- [Bar57] J. Bardeen, L. N. Cooper, and J. R. Schrieffer, Theory of Superconductivity, *Phys. Rev.*, **108**(5), 1175–1204, 1957.
- [Bau18] F. Bauer, *Optimierung von gekoppelten dc-SQUIDs durch die Unterdrückung parasitärer Resonanzen und die Etablierung eines neuen Herstellungsprozesses für Nb/Al-AlO_x/Nb-Josephson-Kontakte*, Masterarbeit, Kirchhoff-Institut für Physik, Universität Heidelberg, 2018.
- [Bau22] Fabienne Bauer, *Rauscharme Stromsensor-dc-SQUIDs mit Impedanzanpassung für metallische magnetische Kalorimeter*, Dissertation, Kirchhoff-Institut für Physik, Universität Heidelberg, 2022.
- [Boy22] STP Boyd, G-B Kim, and S Friedrich, Radio-frequency resonances and damping in metallic magnetic calorimeter sensors, *Journal of Low Temperature Physics*, **209**(3-4), 534–539, 2022.
- [Bru82] J. J. P. Bruines, V. J. de Waal, and J. E. Mooij, Comment on: “DC SQUID: Noise and optimization” by Tesche and Clarke, *J. Low Temp. Phys.*, **46**, 383–386, 1982.
- [Bur04] Andreas Burck, *Entwicklung großflächiger magnetischer Kalorimeter zur energieaufgelösten Detektion von Röntgenquanten und hochenergetischen Teilchen*, Diplomarbeit, Kirchhoff-Institut für Physik, Universität Heidelberg, 2004.
- [Can91] R. Cantor, T. Ryhänen, D. Drung, H. Koch, and H. Seppä, Design and optimization of DC SQUIDs fabricated using a simplified four-level process, *IEEE Transactions on Magnetics*, **2**(2), 2927–2931, 1991.
- [Can96] Robin Cantor, *Dc Squids: Design, Optimization and Practical Applications*, 179–233, Springer Netherlands, Dordrecht, 1996.
- [Cha79] W. H. Chang, The inductance of a superconducting strip transmission line, *Journal of Applied Physics*, **50**(12), 8129–8134, 1979.
- [Cla88] J. Clarke and R. Koch, The Impact of High Temperature Superconductivity on SQUIDs, *Science*, **242**, 217–223, 1988.

- [Cla96] John Clarke, Squid fundamentals, in H. Weinstock (Ed.), *SQUID Sensors: Fundamentals, Fabrication and Applications*, 4–5, Kluwer Academic, Dordrecht, 1996.
- [Cla04] J. Clarke and A. I. Braginski (Ed.), *The SQUID Handbook: Vol. 1, Fundamentals and Technology of SQUIDs and SQUID Systems*, Wiley-VCH, 2004.
- [Dea61] B. S. Deaver and W. M. Fairbank, Experimental Evidence for Quantized Flux in Superconducting Cylinders, *Phys. Rev. Lett.*, **7**, 43–46, 1961.
- [Den16] R. Dengler, Self inductance of a wire loop as a curve integral, 2016.
- [Dru96a] D. Drung, Advanced SQUID read-out electronics, in H. Weinstock (Ed.), *SQUID sensors: Fundamentals, Fabrication and Application*, NATO ASI Series E329. Dordrecht: Kluwer, 1996.
- [Dru96b] D. Drung, F. Ludwig, W. Müller, U. Steinhoff, L. Trahms, H. Koch, Y. Q. Shen, M. B. Jensen, P. Vase, T. Holst, T. Freloft, and G. Curio, Integrated $\text{YBa}_2\text{Cu}_3\text{O}_{7-x}$ magnetometer for biomagnetic measurements, *Appl. Phys. Lett.*, **68**, 1421–1423, 1996.
- [Dru02] D. Drung, High-performance DC SQUID read-out electronics, *Physica C: Superconductivity*, **368**(1-4), 134–140, 2002.
- [Dru06] D. Drung, C. Hinnrichs, and H.-J. Barthelmess, Low-noise ultra-high-speed dc SQUID readout electronics, *Supercond. Sci. Tech.*, **19**(5), S235, 2006.
- [Dru07] D. Drung, C. Abmann, J. Beyer, A. Kirste, M. Peters, F. Ruede, and Th. Schurig, Highly sensitive and easy-to-use squid sensors, *IEEE Transactions on Applied Superconductivity*, **17**(2), 699–704, 2007.
- [Dru11] D. Drung, J. Beyer, J.-H. Storm, M. Peters, and T. Schurig, Investigation of Low-Frequency Excess Flux Noise in DC SQUIDs at mK Temperatures, *IEEE T. Appl. Supercon.*, **21**, 340–344, 2011.
- [Gas17] L. Gastaldo et al., The electron capture in 163ho experiment – ECHo, *The European Physical Journal Special Topics*, **226**(8), 1623–1694, 2017.
- [Enp86] K. Enpuku, K. Yoshida, and S. Kohjiro, Noise characteristics of a dc SQUID with a resistively shunted inductance. II. Optimum damping, *Journal of Applied Physics*, **60**(12), 4218–4223, 1986.
- [Enp91] K. Enpuku and K. Yoshida, Modeling the dc superconducting quantum interference device coupled to the multiturn input coil, *J. Appl. Phys.*, **69**(10), 7295–7300, 1991.

- [Enp92] K. Enpuku, R. Cantor, and H. Koch, Modeling the dc superconducting quantum interference device coupled to the multiturn input coil. III, *J. Appl. Phys.*, **72**(3), 1000–1006, 1992.
- [Ens05] C. Enss (Ed.), *Cryogenic Particle Detection*, Springer-Verlag Berlin Heidelberg, 2005.
- [Fer15] A. Ferring, *Entwicklung von dc-SQUIDs zur Auslesung von metallischen magnetischen Kalorimetern*, Masterarbeit, Kirchhoff-Institut für Physik, Universität Heidelberg, 2015.
- [Fog93] V. Foglietti, K.G. Stawiasz, M.B. Ketchen, and R.H. Koch, Performance of a flux locked series SQUID array, *IEEE T. Appl. Supercon.*, **3**(4), 3061–3065, 1993.
- [Gin50] V. L. Ginzburg and L. Landau, On the theory of superconductivity, *Zh. Èksper. Teoret. Fiz.*, **20**, 1064–1082, 1950.
- [Gro16] R. Gross, A. Marx, and F. Deppe, *Applied Superconductivity: Josephson Effect and Superconducting Electronics*, De Gruyter Textbook Series, Walter De Gruyter Incorporated, 2016.
- [Hen17] Daniel Hengstler, *Development and characterization of two-dimensional metallic magnetic calorimeter arrays for the high-resolution X-ray spectroscopy*, Dissertation, Kirchhoff-Institut für Physik, Universität Heidelberg, 2017.
- [Her23] Matthew Herbst, *High Resolution Magnetic Micro-calorimeters: Thermodynamics, Cooling Requirements, and Noise*, Dissertation, Kirchhoff-Institut für Physik, Universität Heidelberg, 2023.
- [Ina80] Akira Inaba, Superconductive transition point of tantalum and niobium as a reference temperature, *Japanese Journal of Applied Physics*, **19**(8), 1553, 1980.
- [Iva68] Yu. M. Ivanchenko and L. A. Zil’berman, Destruction of Josephson Current by Fluctuations, *ZhETF*, **8**, 113–115, 1968.
- [Jay81] J. M. Jaycox and M. B. Ketchen, Planar coupling scheme for ultra low noise dc SQUIDS, *IEEE Transactions on Magnetics*, **17**(1), 400–403, 1981.
- [Jos62] B. D. Josephson, Possible new effects in superconductive tunnelling, *Physics Letters*, **1**(7), 251–253, 1962.

- [Jos65] B. D. Josephson, Supercurrents through barriers, *Advances in Physics*, **14**(56), 419–451, 1965.
- [Kaa20] Fabian Kaap, *Untersuchung des Einflusses von Kernspins und in Niob gespeichertem Wasserstoff auf das niederfrequente magnetische Flussrauschen in supraleitenden Quanteninterferenzdetektoren*, Master thesis, Kirchhoff-Institut für Physik, Universität Heidelberg, 2020.
- [Kem15] S. Kempf, A. Ferring, A. Fleischmann, and C. Enss, Direct-current superconducting quantum interference devices for the readout of metallic magnetic calorimeters, *Superconductor Science and Technology*, **28**(4), 45008, 2015.
- [Kem18] S. Kempf, A. Fleischmann, L. Gastaldo, and C. Enss, Physics and Applications of Metallic Magnetic Calorimeters, *Journal of Low Temperature Physics*, 1–15, 2018.
- [Ket78] M. B. Ketchen, W. M. Goubau, J. Clarke, and G. B. Donaldson, Superconducting thinfilm gradiometer, *J. Appl. Phys.*, **49**, 4111–4116, 1978.
- [Ket81] M. Ketchen, Dc squids 1980: The state of the art, *IEEE Transactions on Magnetics*, **17**(1), 387–394, 1981.
- [Ket82] M. B. Ketchen and J. M. Jaycox, Ultra-low-noise tunnel junction dc SQUID with a tightly coupled planar input coil, *Applied Physics Letters*, **40**(8), 736–738, 1982.
- [Ket85] A. W. Kleinsasser et al. Ketchen, W. J. Gallagher, Dc squid flux focuser, in H. D. Hahlbohm und H. Lübbig (Ed.) (Ed.), *SQUID'85 Superconducting Quantum Interference Devices and their Applications: Proceedings of the Third International Conference on Superconducting Quantum Devices, Berlin (West), June 25-28, 1985*, 865–871, Walter de Gruyter, 1985.
- [Ket91] M.B. Ketchen, Design considerations for DC SQUIDs fabricated in deep sub-micron technology, *IEEE T. Magn.*, **27**, 2916–2919, 1991.
- [Knu87] J. Knuutila, A. Ahonen, and C. D. Tesche, Effects on DC SQUID characteristics of damping of input coil resonances, *Journal of Low Temperature Physics*, **68**(3-4), 269–284, 1987.
- [Knu88] J. Knuutila, M. Kajola, H. Seppä, R. Mutikainen, and J. Salmi, Design, Optimization, and Construction of a DC SQUID with Complete Flux Transformer Circuits, *Journal of Low Temperature Physics*, **71**(5-6), 369–392, 1988.

- [Koc07] Roger H. Koch, David P. DiVincenzo, and John Clarke, Model for $1/f$ flux noise in squids and qubits, *Phys. Rev. Lett.*, **98**, 267003, 2007.
- [Kra23] Fabian Kraemer, *Development and characterization of an integrated two-stage dc-SQUID for the read-out of metallic magnetic calorimeters*, Bachelor thesis, Kirchhoff-Institut für Physik, Universität Heidelberg, 2023.
- [Kui08] K. H. Kuit, J. R. Kirtley, W. van der Veur, C. G. Molenaar, F. J. G. Roesthuis, A. G. P. Troeman, J. R. Clem, H. Hilgenkamp, H. Rogalla, and J. Flokstra, Vortex trapping and expulsion in thin-film $\text{yba}_2\text{cu}_3\text{o}_{7-\delta}$ strips, *Phys. Rev. B*, **77**, 134504, 2008.
- [Lan60] L.D. Landau, L.P. Bell, E.M. Lifshitz, and J.B. Sykes, *Electrodynamics of Continuous Media*, Volumen 8 in *Course of Theoretical Physics*, Ney York: Pergamon Press, 1960.
- [Lik86] K. K. Likharev, *Dynamics of Josephson Junctions and Circuits*, Gordon and Breach, New York, 1986.
- [Mae95] M. Maezawa, M. Aoyagi, H. Nakagawa, I. Kurosawa, and S. Takada, Specific capacitance of $\text{Nb}/\text{AlO}_x/\text{Nb}$ Josephson junctions with critical current densities in the range of $0.1 - 18 \text{ kA/cm}^2$, *Applied Physics Letters*, **66**(16), 2134–2136, 1995.
- [Man21] Federica Mantegazzini, *Development and characterisation of high-resolution metallic magnetic calorimeter arrays for the ECHo neutrino mass experiment*, Dissertation, Kirchhoff-Institut für Physik, Universität Heidelberg, 2021.
- [Maz24] David Mazibrada, *To be published*, Master thesis, Kirchhoff-Institut für Physik, Universität Heidelberg, 2024.
- [McC68] D. E. McCumber, Effect of ac Impedance on dc Voltage-Current Characteristics of Superconductor Weak-Link Junctions, *Journal of Applied Physics*, **39**(7), 3113–3118, 1968.
- [Mei33] W. Meissner and R. Ochsenfeld, Ein neuer Effekt bei Eintritt der Supraleitfähigkeit, *Naturwissenschaften*, **21**(44), 787–788, 1933.
- [Ono97] R. H. Ono, J. A. Koch, A. Steinbach, M. E. Huber, and M. W. Cromar, Tightly coupled dc SQUIDs with resonance damping, *IEEE Transactions on Applied Superconductivity*, **7**(2), 2538–2541, 1997.
- [Ric17] D. Richter, *Auslesung von SQUIDs mittels Flussrampenmodulation*, Masterarbeit, Kirchhoff-Institut für Physik, Universität Heidelberg, 2017.

- [Ryh92] Tapani Ryhänen, Heikki Seppä, and Robin Cantor, Effect of parasitic capacitance and inductance on the dynamics and noise of dc superconducting quantum interference devices, *Journal of Applied Physics*, **71**(12), 6150–6166, 1992.
- [Sep87] H Seppä and T Ryhänen, Influence of the signal coil on DC-squid dynamics, *IEEE Transactions on Magnetics*, **23**(2), 1083–1086, 1987.
- [Sta93] K. G. Stawiasz and M. B. Ketchen, Noise Measurements of Series SQUID Arrays, *IEEE T. Appl. Supercon.*, **3**, 1808–1811, 1993.
- [Ste68] W. C. Stewart, Current-Voltage Characteristics of Josephson Junctions, *Applied Physics Letters*, **12**(8), 277–280, 1968.
- [Tes77] C. D. Tesche and J. Clarke, dc SQUID: Noise and Optimization, *Journal of Low Temperature Physics*, **294**(3), 1–9, 1977.
- [Tie21] Eite Tiesinga, Peter J. Mohr, David B. Newell, and Barry N. Taylor, Co-data recommended values of the fundamental physical constants: 2018, *Rev. Mod. Phys.*, **93**, 025010, 2021.
- [Wel93] R.P. Welty and J.M. Martinis, Two-stage integrated squid amplifier with series array output, *IEEE Transactions on Applied Superconductivity*, **3**(1), 2605–2608, 1993.